12-2016

Multiscale Mechanics of Bone: Examining the Influence of Genetic Alterations

Brendyn James Miller

Multiscale Mechanics of Bone: Examining the Influence of Genetic Alterations

by

Brendyn James Miller

A thesis submitted to the College of Engineering
Florida Institute of Technology
in partial fulfillment of the requirements
for the Degree of

Master of Science
in
Biomedical Engineering

Melbourne, Florida
December, 2016

We the undersigned committee hereby approve the attached thesis, “Multiscale Mechanics of Bone: Examining the Influence of Genetic Alterations” by Brendyn James Miller.

_____

Advisor
Title
College

_____

Advisor
Title
College

_____

Advisor
Title
College

Abstract

Title: Multiscale Mechanics of Bone: Examining the Influence of Genetic Alterations

Author: Brendyn James Miller

Advisor: Alessandra Carriero, Ph.D.

This MSc thesis investigates how genetic alterations involved in the synthesis of proteins or in the regulation of tissue remodeling affects the composition, structure and mechanics of bone at the multiscale levels. This was accomplished by performing two mouse model studies. In the first study, bone properties of TIMP-3 knock-out (*Timp-3*$^{-/-}$) mice were examined by performing mechanical testing, μCT analysis, and FTIR analysis. Results demonstrated that the mechanical integrity of the *Timp-3*$^{-/-}$ bone was compromised. Decreased values for the yield and ultimate load, stress capacity, and fracture toughness were observed in both the TIMP-3 deficient bones. These reductions in the mechanical and material properties were attributed to alterations in the bone structure and composition. The *Timp-3*$^{-/-}$ cortical bone was less dense, thinner, and exhibited increase porosity and the trabeculae in the cancellous bone were thinner, more interconnected, and more tightly packed together. The composition of the *Timp-3*$^{-/-}$ bone were found to have altered mineralization and increased compositional heterogeneity. These geometric and compositional changes suggest that there is increased bone remodeling, possibly due to increased matrix metalloproteinase (MMP), disintegrin-metalloproteinase (ADAM), and disintegrin and metalloproteinase with thrombospondin-like motifs (ADAMTS) activity, resulting from a lack of TIMP-3.

These results therefore suggest that TIMP-3 is crucial for maintaining optimal bone tissue during growth and development.

In the second study, the cochlear intracortical structure of genetically modified *oim* mice, a mouse model of osteogenesis imperfecta (OI) or brittle bone disease, was examined to gain insight on the possible causes of hearing loss, typical in severe cases of the disease. The results from the image analysis demonstrate that the *oim* bone is much more porous with more populated and interconnected canals within the cochlea. This higher porosity, possibly due to high bone turnover in these mice, may lead to reduced bone fracture toughness, thus increasing the risk of consequent bone deformities and the likelihood of hearing loss.

Both studies showed how genetic mutations at the nano-scale level can result in reduced mechanical properties of the bone at the macro-scale level. It is therefore crucial to correct any biological alterations at any level of the hierarchy to maintain the healthy bone structure. These studies provide a deeper understanding of the bone material and will ultimately lead to the development of new treatments for skeletal pathologies.

Table of Contents

List of Figures

List of Tables

Acknowledgement

I would like to express my gratitude towards my advisor, Prof. Alessandra Carriero, for giving me the opportunity to perform the studies presented in this thesis and for her wisdom, patience, and encouragement in guiding me through this process. I would also like to thank Maria Sagastume, Carlos Brito Gomez, and Giancarlo Bennardo for their assistance in pre-processing the synchrotron computed tomorgraphy - images that were analyzed in this study. Furthermore, I would like to thank Prof. Ted Conway and Prof. Razvan Rusovici for reviewing the work outlined in this thesis. Finally, I would like to thank my parents, Chris and Leslie Miller, for their unwavering support and encouragement through my entire graduate school experience.

Dedication

To my Lord and Savior, Jesus Christ, whose example as a Healer inspired me to go into the medical field in the hope that my work could bless the lives of others through the healing of their bodies.

Chapter 1

Introduction

1.1 Thesis Background and Motivation

Bone is a complex organ that exhibits a hierarchical structure. The mechanical properties of the bone at the whole bone, or macro-scale level, depend on the bone architecture at the tissue, or micro-scale level, and on the arrangement of collagen (protein) and hydroxyapatite (mineral) constituents at the molecular, or nano-scale level. The arrangement of primary molecular constituents at the nano-scale level are due to the coordinated activity of physiological factors that are the end products of biological pathways programed by genetic information contained in DNA and RNA molecules. It is this hierarchical structure that gives bone both high strength and toughness, a desirable combination for all materials. Furthermore, bone can adapt to mechanical loading and change its mass, shape, and properties in response to its mechanical environment.

However, aging and disease change bone structure and composition and effect its function, having a dramatic effect on the mechanics of the whole bone. Prior research has also shown that genetic changes can alter the expression of biological factors that influence the structure and composition of bone. In some cases, genetic alteration can completely disrupt the production of certain proteins or other biological molecules that play a role in coordinating how the bone is formed, indirectly altering the structure of the bone. For example, in one study, investigators looked at how suppressing a specific proteinase, tissue inhibitor of metalloproteinases-3 (TIMP-3), altered bone structure.(Javaheri et al., 2016) The results of their research demonstrated that TIMP-3 deficiency correlated with a reduction

in overall bone mass and size. In other cases, genetic variations change how the proteins from which bone is formed are synthesized, directly compromising its structural integrity. For example, osteogenesis imperfecta (OI) is a skeletal disorder in which alterations in the COL1A1 and COL1A2 genes reduce either the amount or the quality of type 1 collagen in bones and other connective tissue. Because of their hierarchical structure, these changes also reduce the amount and/or the quality of the bone. These genetic mutations increase the risk of bone fracture in patients with OI.

In both TIMP-3 deficiency and OI, there are correlations between genetic changes and altered bone structure. However, a complete understanding of how the bone structure changes because of genetic alterations remains elusive. In the first case, it is known that TIMP-3 deficiency alters the bone structure, but exactly how the bone mechanics, morphology, and composition change remains in question. In the second case, it is known that OI alters bone structure and causes hearing loss, but exactly how the bone structure changes and contributes to hearing loss is still unknown.(Riedner, Levin, & Holliday, 1980; Swinnen, De Leenheer, Coucke, Cremers, & Dhooge, 2009) Therefore, the goal of this thesis is to examine how the properties of both TIMP-3 deficient bone and OI bone change to gain a more thorough understanding of bone biology and mechanics with the ultimate goal of developing successful therapies for skeletal pathologies.

1.2 Hypothesis and Thesis Outline

A comprehensive understanding of bone mechanics requires basic knowledge of how to evaluate and interpret bone properties at each scale of the bone hierarchy. Chapter 2 introduces bone composition, structure, and mechanics, with methods for the characterization of these properties and

with a special interest in mouse bone. Chapters 3 and 4 explore how two different gene modifications affect the bone hierarchy and alter its integrity.

Many studies examining the function of TIMP-3 have found that TIMP-3 deficiency adversely affects tissue integrity (Brew & Nagase, 2010; Cruz-Munoz, Kim, & Khokha, 2006; Cruz-Munoz, Sanchez, et al., 2006; Federici et al., 2005; Gill, Pape, Khokha, Watson, & Leco, 2003; Janssen et al., 2008; Kassiri et al., 2005; Leco et al., 2001; Mohammed et al., 2004; Sahebjam, Khokha, & Mort, 2007). For example, in one study researchers examining the lungs of TIMP-3 knock out (*Timp-3*$^{-/-}$) mice found that TIMP-3 deficiency resulted in excessive extracellular matrix (ECM) degradation that resulted in illness and premature death (Leco et al., 2001). In another study, scientists observed that TIMP-3 deficiency caused increased collagen and aggrecan degradation in *Timp-3*$^{-/-}$ mice (Sahebjam et al., 2007). In each of these cases, as well as others, TIMP-3 deficiency had an adverse effect on the tissue being examined. However, to the best of my knowledge, no studies have been conducted which investigate the effects of TIMP-3 deficiency on bone properties. Therefore, the first aim of this thesis was to perform mechanical, geometric, and compositional testing on *Timp-3*$^{-/-}$ mouse bone to quantify how the bone changes because of TIMP-3 deficiency.

The first hypothesis of this thesis is that genetic suppression of the TIMP-3 gene deteriorates the mechanics of bone by changing its structure and composition.

Chapter 3 reports the results of a study in which bones from *Timp-3*$^{-/-}$ mice were examined at the nano-, micro-, and macro-scale lengths to determine how TIMP-3 deficiency affects the mechanical, geometric, and compositional properties of bone. Characterizing TIMP-3 gene-related changes in bone properties will help in understanding the role of this gene

in determining the overall mechanical integrity of the bone through changes in its geometry and composition.

In several skeletal pathologies, compositional and structural changes lead to alterations in bone toughness. In osteogenesis imperfecta bone, for example, collagen modifications detrimentally affect its hierarchical structure and mechanics, making the bone more prone to fracture. Bone's micro-porosity has an influence on the propagation of cracks at the micro-scale level (Alessandra Carriero et al., 2014) and on the overall toughness of the bone (A. Carriero, M. Doube, et al., 2014; Yeni, Brown, Wang, & Norman, 1997). Additionally, osteogenesis imperfecta bone exhibits altered intra-cortical porosity (A. Carriero, M. Doube, et al., 2014; Vardakastani et al., 2014).

The second hypothesis is that altered intra-cortical porosity also characterizes the cochlea in OI, which may affect the mechanical integrity of the bone and possibly contribute to the hearing loss associated of severe conditions of the disease.

In chapter 4, the structure of the cochlea in a mouse model genetically modified to express mild to severe osteogenesis imperfecta was investigated. The geometry and morphology of the cortical bone, intracortical canals, and lacunae were examined by analyzing reconstructed 3-D computed models of images obtained using synchrotron computed tomography (SR-CT). Quantifying geometric differences in the bone affected by OI will help provide insight into understanding how the mechanics of the bone are altered.

Finally, chapter 5 summarizes the main outcomes of this thesis, presenting the contributions of this new knowledge to the field of bone mechanics as well as perspectives for future research.

Chapter 2:

Bone Quality and Quantity

2.1 Introduction

This chapter provides a brief overview of bone function, a descriptive summary of bone composition and structure, as well as a presentation of how the mechanical, geometric, and compositional properties can be evaluated to determine bone quality and quantity. By the conclusion of this chapter, the reader should be able to understand the basic bone anatomy and terminology that will be used in future chapters to describe the principal procedures and findings presented in this text.

2.2 Bone Function

Bone is a fascinating organ that performs a variety of mechanical and metabolic functions within the body. Bones in the body, which are collectively known as the skeleton, act as a structural support system, providing a rigid frame where muscles, tendons, and ligaments can attach to and act on to generate forces which enable the body to move freely in three-dimensional space. Furthermore, bone preserves and protects internal organs such as the brain, heart, and lungs by acting as a casing that supports the organ and protects them from physical trauma. Bones also enable vertebrates to hear sounds by playing a role in sound transduction via the middle ear, allowing for sound vibrations to be transferred from the ear drum to the cochlea. Additionally, bone contains the bone marrow, which produces new blood cells and stem cells and acts as a material reservoir for minerals such as calcium and phosphate (Ethier & Simmons, 2007).

2.3 Bone Composition

2.3.1 Composition Overview

Bone is a composite structure consisting primarily of mineralized type I collagen fibrils, calcium hydroxyapatite ($Ca_{10}(PO_4)_6(OH)_2$) crystals, and water (Steve Weiner & Wagner, 1998). Up to over 200 other non-collagenous proteins (NCPs) can also be present in bone; however, these proteins consist of less than 10% of bone composition and have very little impact on how the bone functions mechanically (Delmas, Tracy, Riggs, & Mann, 1984). These three major components and the trace amounts of NCPs combine to form the two types of bone tissue: lamellar and woven bone. The combination of these two bone tissue types are found in both kinds of bone found within the body: cortical and trabecular bone. While both types of bone have a similar composition; consisting of lamellar and woven bone. The distinction between the two types of bone is due to differences in their respective apparent densities and their microarchitecture. Trabecular bone is much more porous, having an apparent density that ranges typically from 0.21 to 0.3 g/cm^3 while the apparent density of the more compact cortical bone has been traditionally reported as having an average value of 1.86 g/cm^3 (Keaveny & Hayes, 1993). Furthermore, trabecular bone forms a network of interconnected struts which help support and redistribute stresses throughout the bone, while cortical bone forms the outer shell and serves as the primary load bearing unit. The combination of both trabecular and cortical bone components enable the entire bone to optimize its strength-to-weight ratio which enables it to optimize its role in the skeletal system.

2.3.2 Type I Collagen Fibrils

Type I collagen makes up roughly 20% of the total bone mass and consists of three polypeptide chains (2 pro-α1 molecules and 1 pro-α2 molecule) that bind together to form a heterotrimeric, triple helical structure known as tropocollagen (Figure 1) (Ethier & Simmons, 2007).

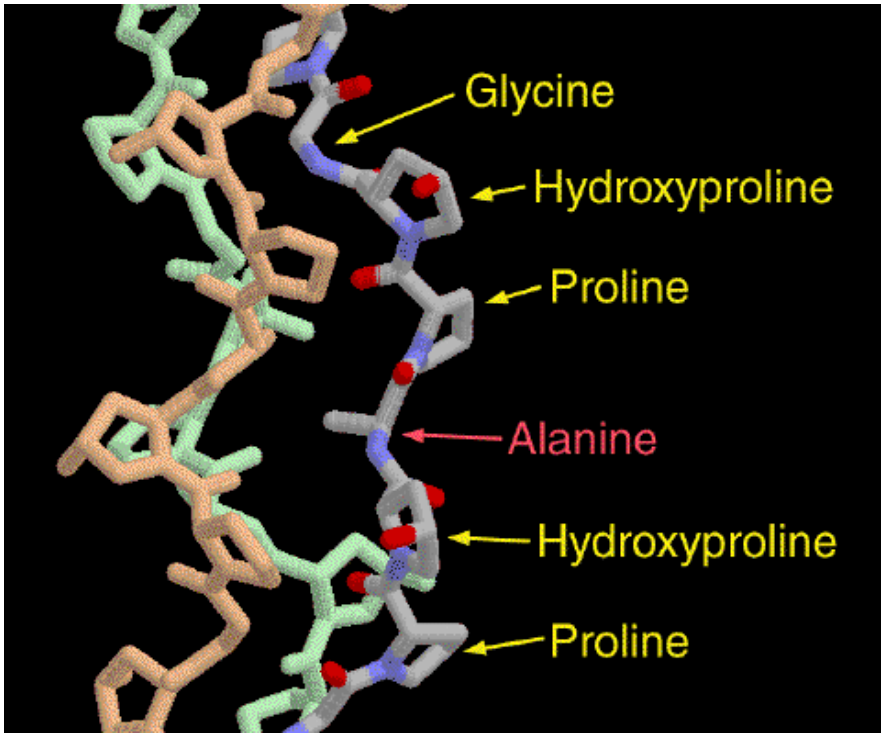

Figure 1. Schematic of the triple helical structure of tropocollagen ("Collagene,").

Both molecules have a common repeating amino acid motif of Glycine – X – Y, where X and Y are typically proline and hydroxyproline (Rich & Crick, 1955). Collectively, tropocollagen is comprised of 1,014 amino acids and is approximately 1.5 nm in diameter and 300 nm in length (Miller, 1984). Micro-fibrils are constructed from neighboring strands of tropocollagen that are covalently cross-linked (Figure 2).

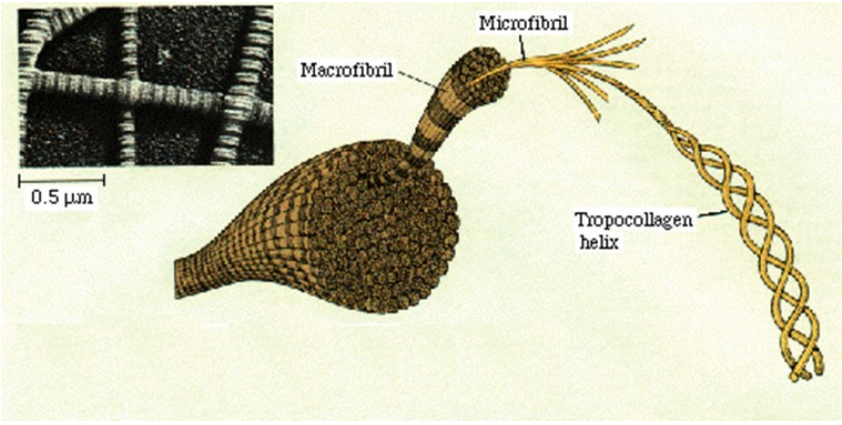

Figure 2. Schematic of tropocollagen packed within a micro-fibril ("Introduction of Human Physiology Part2,").

The packing formation of the tropocollagen within the micro-fibril is worth noting, as the collagen molecules are aligned parallel to one another with small, 35 nm gaps existing between the ends of each chain (Figure 3).

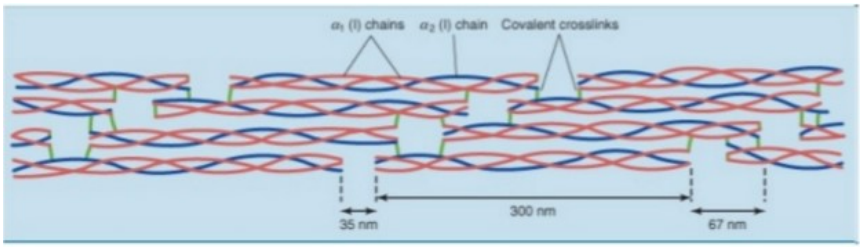

Figure 3. Packing formation of tropocollagen within a micro-fibril. The tropocollagen molecules are bound together by covalent crosslinks, with the ends of each tropocollagen spaced 35 nm from the following tropocollagen strand and offset by 67 nm from the adjacent tropocollagen strand ("Extracellular matrix,").

Additionally, the gap existing between each type I collagen from one column within the fibril to the neighboring column is offset by approximately 68 nm (Hodge & Petruska, 1963). The micro-fibrils then

aggregate to form macro-fibrils and likewise, the macro-fibrils bind together to form collagen fibers. While the exact role that type I collagen plays in determining bone strength has yet to be fully understood, it has been noted that this component of the bone matrix is crucial for providing the bone with ductility and toughness (i.e. the ability to absorb energy) (Viguet-Carrin, Garnero, & Delmas, 2006).

2.3.3 Hydroxyapatite Crystals

Hydroxyapatite crystals act as the mineral component of the bone matrix and account for 70% of the total bone mass (Ethier & Simmons, 2007). These crystals are characterized as thin plates that are approximately 50 nm in length and 25 nm in width, with thicknesses that have been shown to vary with maturation from 1.5 nm to 4.0 nm (Figure 4) (Lowenstam & Weiner, 1989).

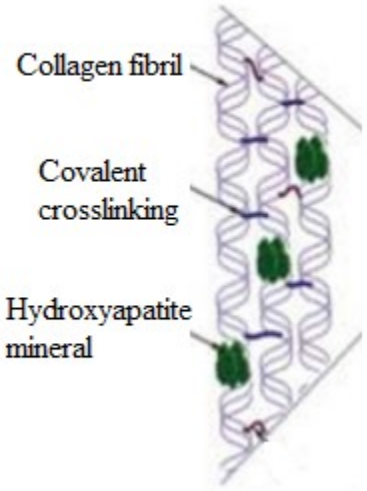

Figure 4. Diagram depicting the plate-like hydroxyapatite crystals (shown in green) mineralized in the spaces between collagen fibrils. The hydroxyapatite crystals are typically 50 nm in length, 25 nm in width, and 1.5 to 4.0 nm thick ("Characterizing the mechanical properties of bone with the assistance of digital light microscopy,").

These crystals mineralize within the spaces of the collagen fibrils and increase in size as the bone ages. This increase in crystal size is due to crystal aggregation in a process known as secondary nucleation (Augat & Schorlemmer, 2006). These crystals provide the bone with its rigidity and load bearing capability, but also cause the bone to become more brittle as the crystals increase in size (Viguet-Carrin et al., 2006). Therefore, a balance between small crystals from newly formed bone and larger crystals from older bone is considered optimal for healthy bone.

2.3.4 Water

The remaining 10% of the bone mass consists of water (Ethier & Simmons, 2007). Water fills gaps within the collagen fibrils and plays an important role in dictating the mechanical behavior of the bone by directly altering its strength, toughness, and stiffness (Nyman et al., 2006).

2.4 Bone Structure

Bone structure can be characterized as hierarchical in nature, with the composition of the collagen-mineral components of bone at the nano-scale (nm) influencing the structure of the bone tissue at the micro-scale (μm) which, in turn, impacts the mechanical and material properties of the entire bone at the macro-scale (mm) (Figure 5).

2.4.1 Nano-Scale: Mineral and Collagen organization

The primary constituents of bone at the nano-scale level (nm) are organic collagen fibrils with a small number of proteoglycans and non-collagenous proteins that are interlaced with inorganic hydroxyapatite crystals. The plate-like hydroxyapatite crystals are formed on the surface of the fibrils such that they are oriented parallel to the direction of the fibrils and are arranged periodically between the ends of the collagen fibrils (Figure 4) (Stephen Weiner & Traub, 1986)

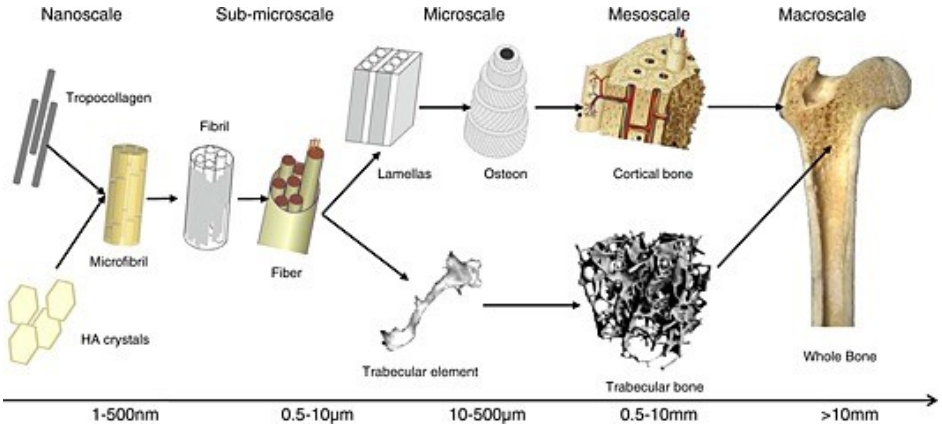

Figure 5. Schematic of the hierarchical structure of bone (Barkaoui, Chamekh, Merzouki, Hambli, & Mkaddem, 2014).

2.4.2 Micro-Scale: Bone Tissue

At the micro-scale level (µm), bone consists of two types of bone tissue: woven and lamellar bone (Figure 6).

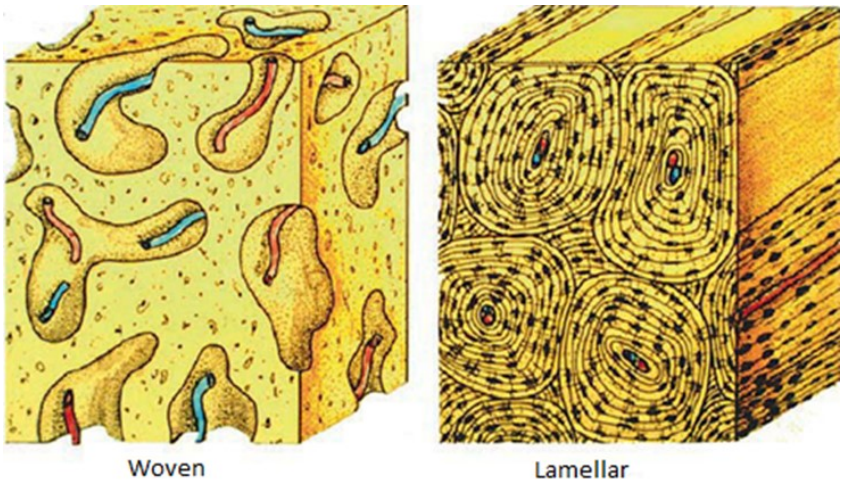

Figure 6. Comparison of woven and lamellar bone. The woven bone is rapidly deposited and is therefore poorly organized. The lamellar bone is developed over time and is highly organized (Safadi et al., 2009).

Woven bone tissue is deposited very rapidly during periods of accelerated bone growth or production and is very poorly organized. The

orientation of the collagen fibers and minerals seems to be randomly arranged, which would decrease the mechanical properties of the woven bone if it were not offset by increases in mineralization that are typically seen in this type of bone. Alternatively, lamellar bone is formed slowly over time and is arranged very specifically into thin layers of densely packed collagen fibers and mineral crystals that are organized parallel to one another. These layers are approximately 3-7 μm thick and are referred to individually as lamellae (Steve Weiner, Traub, & Wagner, 1999). The lamellae are then built up in a stack in a fashion that is like that of a plywood board. Each lamellae is oriented at a right angle to its neighbors and helps provide the bone with increased strength. Woven bone is formed initially during bone development and is gradually replaced by lamellar bone.

2.4.3 Macro-Scale: Bone as an Organ

Bone is either classified as cortical (compact) or trabecular (spongy) bone at the macro-scale level (mm) (Figure 7).

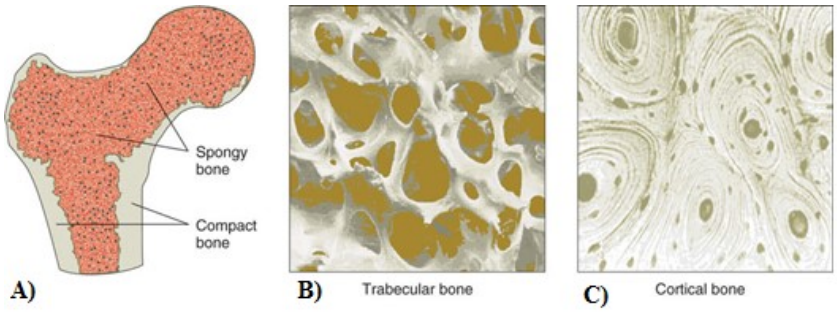

Figure 7. A) Artistic representation of the femoral head depicting both the cortical (compact) and trabecular (spongy) bone. **B)** Image depicting trabecular bone. **C)** Image depicting cortical bone ("Bone Structure and Function,").

Cortical, also known as compact bone, has a very complex lamellar microarchitecture (Figure 8).

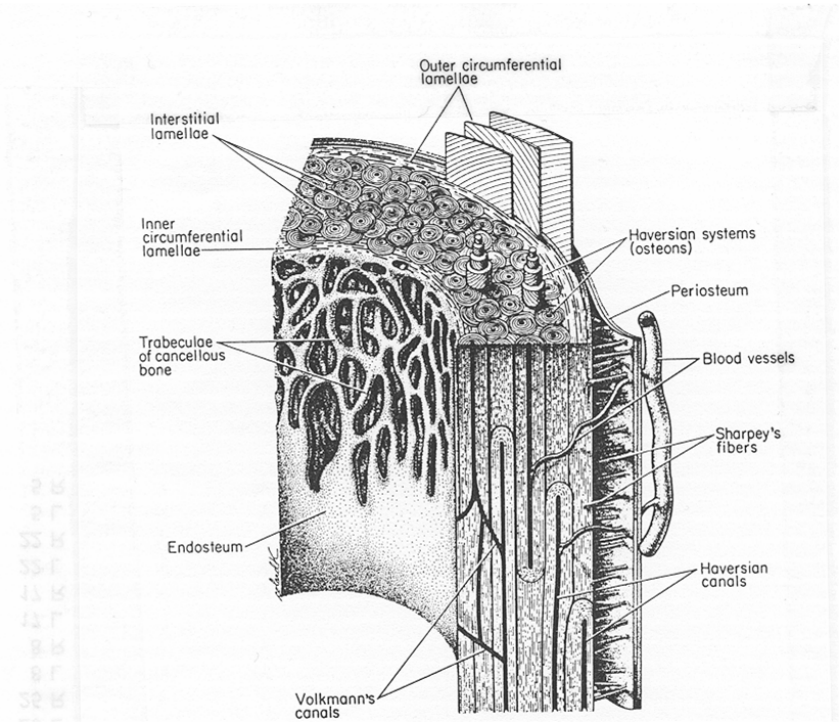

Figure 8. Schematic of cortical bone depicting all the major anatomical structures ("bonestructure.gif (GIF Image, 823 × 703 pixels),").

The orientation of the lamellae differs depending on its location in the bone. The lamellae located on the outer and inner surfaces of the cortical bone are oriented parallel to one another and line the inner and outer circumference of the bone. The lamellae are aptly named circumferential lamellae. Between the inner and outer circumferential lamellae there are two other lamellar-based structures: the osteonal bone and the interstitial lamellar bone. The osteonal bone consists of lamellae that are oriented parallel to each other and are arranged in concentric rings to form cylindrical tubes that are about 200 μm in diameter and 1 cm in length. Packed in-between the osteonal bone and the inner and outer

circumferential lamellae is the interstitial lamellar bone. These layers of lamellae consist of partially resorbed osteonal bone that fills in the empty spaces in the bone matrix. Finally, cortical bone contains a complete network of canals through which extracellular fluid can flow and allow nutrients be dispersed to the cells occupying the bone matrix. These canals are known as haversian canals and consist of blood vessels that are lined with concentric lamellae. The haversian canals are typically oriented along the long axis of the bone and are connected to one another through canals called Volkmann's canals which are oriented along the radial axis of the bone. Because cortical bone is much more compact than trabecular bone, it accounts for approximately 80% of the overall weight of bone and imbues the bone with much of its strength and rigidity which provides the bone with its supportive and protective functions (Iolascon et al., 2013).

Trabecular bone, also known as cancellous bone, is the other major type of bone and is commonly found in the vertebrae, flat bones, and ends of long bones. As mentioned previously, trabecular bone is much more porous and its structure differs significantly from cortical bone (Figure 9). Trabecular bone is constructed from a framework of interconnected rods and plates known collectively as trabeculae. Most trabeculae have an average thickness of 200 μm. Like the osteons in the cortical bone, the trabeculae are constructed from concentric lamellae. The spaces between the trabeculae are large and account for its significantly decreased density; trabecular bone is traditionally characterized as 75% - 95% porous. However, the number of trabeculae, the spacing between trabeculae, the shape of the trabeculae, and the overall orientation of the trabeculae can change depending on the anatomical location, biomechanical function, and age of the subject.

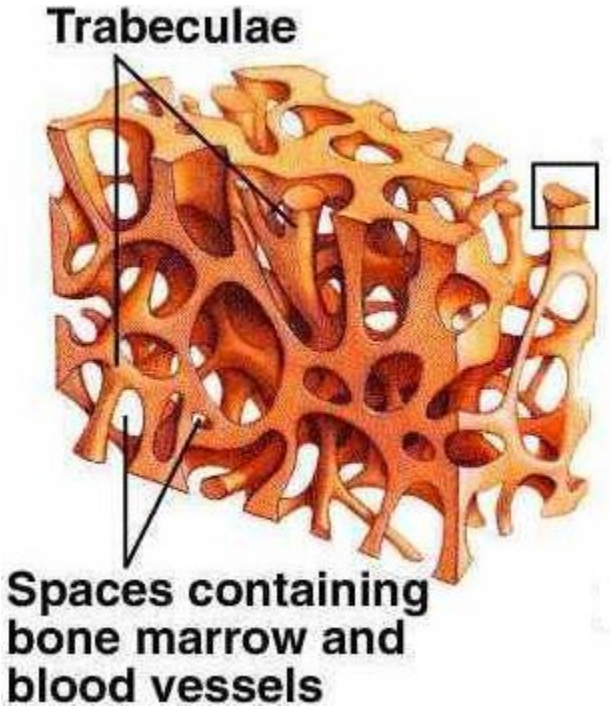

Figure 9. Drawing depicting the interwoven network of trabeculae and the spaces containing the bone marrow and blood vessels in trabecular (spongy) bone ("Pix For > Cancellous Bone Tissue,").

As a result, the density and mechanical properties of the bone can vary significantly (Ethier & Simmons, 2007). Because of its network of plates and rod shaped trabeculae, trabecular bone provides the overall bone organ with the optimal combination of maximum strength and minimal weight.

Both cortical and trabecular bone provide insight into understanding the overall bone structure, and are therefore important to consider when evaluating differences between the two groups of bone. Thus, in this study, the properties of both cortical and trabecular bone were evaluated.

2.5 Bone Formation and Remodeling

The process of forming new bone is known as ossification. There are two types of ossification that occur within the body: intramembranous ossification and endochondral ossification.

Intramembranous ossification is primarily responsible for the formation of the flat bones in the skull, mandible, maxilla, and clavicles and is the process by which new bone tissue is formed in mesenchyme, an embryonic connective tissue. This process occurs in a series of subsequent steps (Figure 10).

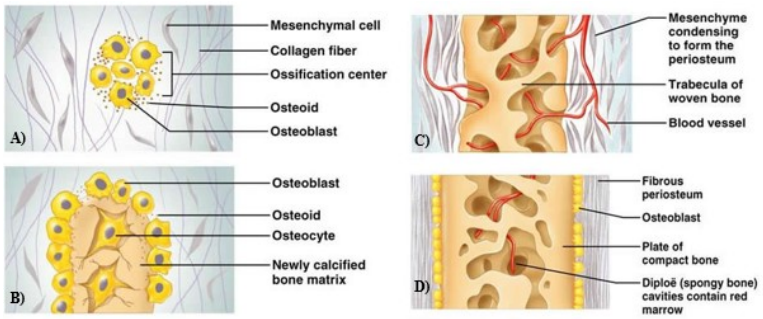

Figure 10. The process of intramembranous ossification. **A)** Osteoprogenitor cells form an ossification center and differentiate into osteoblasts which secrete osteoid **B)** The osteoid calcifies and connects to form new bone **C)** The new bone forms a network of trabecular that is interwoven with blood vessels and mesenchyme condenses on the edges of the bone to form periosteum **D)** The trabecular bone on the outer edges of the bone thicken and form woven bones that is eventually reorganized into lamellar bone("Chapter 6: Bones and Skeletal Tissues,").

First, osteoprogenitor cells aggregate and differentiate into osteoblasts. These osteoblasts release an un-mineralized organic matrix called osteoid. Next, the osteoid combines with calcium and becomes mineralized, forming

branches of calcified bone called spicules. Then, as osteoblasts continue to lay down new osteoid, the spicules grow and eventually connect with one another, creating a network of trabeculae which form the porous structure known as cancellous or trabecular bone. Finally, as the network of trabeculae continues to grow, ossification within the inner region of the cancellous bone begins to slow while the mesenchyme lining the edges of the cancellous bone condenses and forms into a fibrous substance known as periosteum. As osteoblasts on the periphery of the cancellous bone continue to produce osteoid, the trabeculae thicken and eventually form interconnected layers of woven bone. This woven bone is then reorganized into lamellar bone.

Endochondral ossification occurs in bones other than the flat bones and is the process by which new bone tissue is formed from an initial hyaline cartilage model (Figure 11). Initially during development, rods of condensed mesenchyme are formed which act as a template for the bone. These rods are replaced with hyaline cartilage. This cartilage model grows in length due to the activity of chondrocytes. Chondrocytes produce an extracellular matrix which is added to the surface of the cartilage model, enabling it to grow and thicken. As the cartilage model grows, the perichondrium, or the condensed mesenchyme tissue surrounding the cartilage model, matures and becomes vascularized, transitioning into periosteum. The periosteum contains osteoprogenitor cells which differentiate into osteoblasts. These osteoblasts secrete osteoid, which lines the outer diaphysis of the cartilage model. The osteoid then calcifies, forming a collar around the cartilage model made of cortical bone. As mineralized bone forms around the cartilage, nutrients are unable to reach the chondrocytes trapped within the newly formed bone and eventually apoptosis occurs.

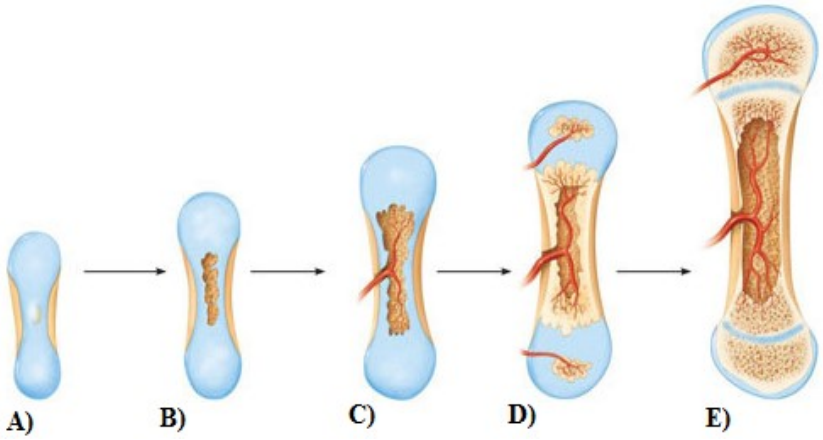

Figure 11.Schematic describing the process of endochondral ossification. **A)** Hyaline cartilage template is formed and grows in length due to chondrocyte activity **B)**Osteoblasts secrete osteoid on 0the outer edge of the template, forming a bone collar around the model. **C)** The inner region of the template begins to degrade and is invaded by blood vessels to form the periosteal bud. **D)** The periosteal bud grows as the cartilage is degraded and replace by bone. **E)** The epiphyses continue to grow, causing the bones to elongate until the epiphyses are completely converted to bone ("Gallery For > Intramembranous Ossification Diagram,").

The inner cartilage begins to degrade, creating space within the bone that is invaded by blood vessels and a vascular connective tissue bud that forms in the center of the cartilage template that is called the periosteal bud. These blood vessels bring in important components such as nutrients, osteoblasts, and osteoclasts. The periosteal bud acts as the primary ossification center where osteoblasts begin laying down fresh osteoid that eventually replaces the cartilage and forms cancellous or trabecular bone. Over time, the cartilage model is replaced with bone. The ends of the model, called the epiphyses, continue to grow and elongate as new cartilage is laid down by chondrocytes. This allows the bones to grow and elongate.

Eventually, when the bone reaches maturity, the cartilage is completely replaced by bone.

Bone remodeling is the process by which old bone is broken down and replaced by new bone (Figure 12). This process occurs continually throughout life and enables the bone to heal from injures such as fractures and micro damage. It also enables the bone to adapt its structure in response to its mechanical load bearing requirements. The ability to replace old or worn out bone with fresh, new bone is crucial to maintaining bone strength and structural integrity. The process in which old bone is broken down is called bone resorption, and the process by which new bone is formed is called bone deposition. These activates are performed by osteoclasts and osteoblasts, respectively. In healthy bone, there is a balance between the rates of bone deposition and bone resorption. There are several factors which effect these roles of bone formation and degradation which involve genetic, mechanical, vascular/nerve, nutritional, and hormonal factors as well as local factors such as growth factors, cytokines, and bone matrix proteins. Diseases or disorders which influence these factors can have a negative impact on bone remodeling, resulting in skeletal anomalies that reduce bone strength and increase the risk of bone fracture due to changes in bone structure and composition. Thus, a balanced rate of bone remodeling is critical in maintaining good bone health.

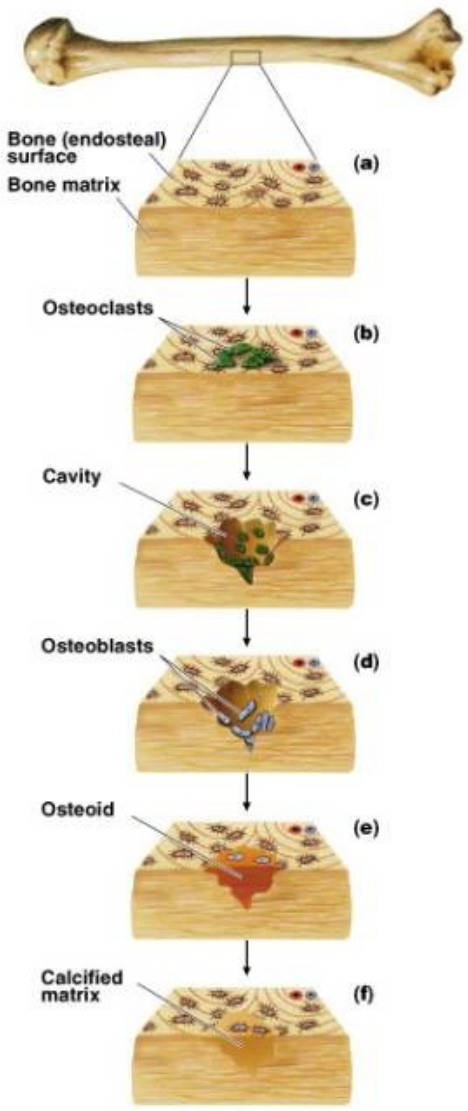

Figure 12. Schematic summarizing the stages of the bone remodeling process **A)** Initially, old bone is damaged. **B)** Then, osteoclasts are activated by biological stimuli such as cytokines and hormones. **C)** The osteoclasts aggregate at the sight of the damaged bone and begin to break down the bone by latching on to the bone and secreting a proteinase enzyme called cathepsin k. This creates a cavity, or resorption pit, in the bone. **D)** The osteoclasts leave the pit, and osteoblasts migrate in and line the surface. **E)** The osteoblasts fill the resorption pit with osteoid. **F)** The osteoid mineralizes, forming new bone ("New Page 1,").

2.6 Bone Cells

Bone is maintained through a process known as bone remodeling. During bone remodeling, old or damaged bone is broken down and replaced with fresh bone. This process is crucial to preserving the structural integrity of bone because it removes defects from the bone that would cause it to fracture. Bone remodeling is accomplished through the coordinated effort of three primary types of bone cells: osteoclasts, which dissolve bone, osteoblasts, which synthesize new bone, and osteocytes, which are permanently encapsulated in the bone ECM and serve to transmit signals to other cells through the bone and help to regulate osteoblasts and osteoclast activity (Van Bezooijen, Papapoulos, Hamdy, Ten Dijke, & Löwik, 2005). Osteoclasts are large multinucleate cells that are composed from multiple combined macrophages. Under the direction of cytokines, these cells latch onto the bone at specific regions where the bone needs to be degraded, and they release enzymes which break down the bone tissue, leading to bone resorption. Osteoblasts, on the other hand, are relatively small, mononucleate cells which have differentiated from osteoprogenitor cells. They line the internal and external edges of the bone, such as the periosteum and the endosteum. As osteoblasts lay down new bone, called osteoid, it can become encapsulated and trapped within the bone. When this happens, the osteoblast will differentiate even further into the third type of bone cells: osteocytes. Despite being immobilized within the bone, the osteocytes are still able to communicate with other osteocytes by forming connected branches that are extend through small pathways in the bone called canaliculi. These cells generate cytokines such as growth factors which promote bone remodeling by triggering osteoblast and osteoclast activity.

2.7 Bone Quality and Quantity

Bone quality and quantity are often used as measures of bone health (Bouxsein, 2005). The latter is simply a measure of the amount of bone, while the former is much more complex and involves several interdependent aspects of the bone structure, composition and mechanics such as microarchitecture, mineralization, microdamage, and matrix and mineral composition (Compston, 2006). These factors are primarily influenced by bone turnover, the process through which old bone is resorbed and new bone is formed (Compston, 2006).

2.7.1 Bone Quantity

Bone quantity, or the amount of bone, is typically evaluated by measuring the bone mineral density (BMD) or the bone mineral content (BMC). These measurements can be assessed using either invasive or non-invasive methods. The primary invasive method used to determine bone quantity is called bone ashing and involves heating the bone to break down and remove the organic components of the bone to isolate the inorganic or mineralized portion of the bone that can be used to measure BMD (Haba et al., 2012). For the non-invasive methods, the primary tests include dual-energy X-ray absorptiometry (DEXA), ultrasound (US), and quantitative computer tomography (QCT) (Babatunde, Fragomen, & Rozbruch, 2010). DEXA is a two-dimensional technique that uses x-rays at different energy intensities to determine both BMD and BMC of a patient in vivo. Ultrasound is used to evaluate new bone formation; however, this technique is not very accurate and therefore not used very often. QCT uses x-ray computed tomography to construct two-dimensional or three-dimensional images that can be used to evaluate BMD and BMC.

2.7.2 Bone Quality

Bone quality can be evaluated in terms of bone strength and bone fracture toughness. Bone strength is the bone's ability to resist deformation and failure, while bone fracture toughness is a measure of the ability of bone to resist fracture propagation. Through the course of both clinical and scientific studies, researchers have developed multiple parameters to measure bone strength and toughness, and have related these to the architectural and compositional properties of the bone. Each of these bone properties have a variety of different analytical techniques that allow measurements to be taken at different scale lengths, ranging from the nano-scale to the macro-scale level.

2.7.2.1 Bone Mechanical and Material Properties

Bone Strength

Bone strength is a metric used to describe the bone's resistance to deformation and can be evaluated by quantifying the mechanical and material properties of the bone. Traditional bone strength metrics include such measurements as the yield and ultimate loads, and stiffness. Material properties include measures like the yield and ultimate stress and Young's modulus and are used to provide important insight and understanding of bone load bearing capacity.

Bone Toughness

The toughness of bone represents the amount of energy or work required to deform the bone. The amount of energy required to deform the bone past its yield point is denoted as the work to yield while the amount of energy required to fracture the bone is referred to as the work to fracture. The work to yield is typically measured quantitatively as the area under the load-deformation curve within the elastic region, while the work to fracture is the area under the entire load-deformation curve (Figure 13) (Turner & Burr, 1993).

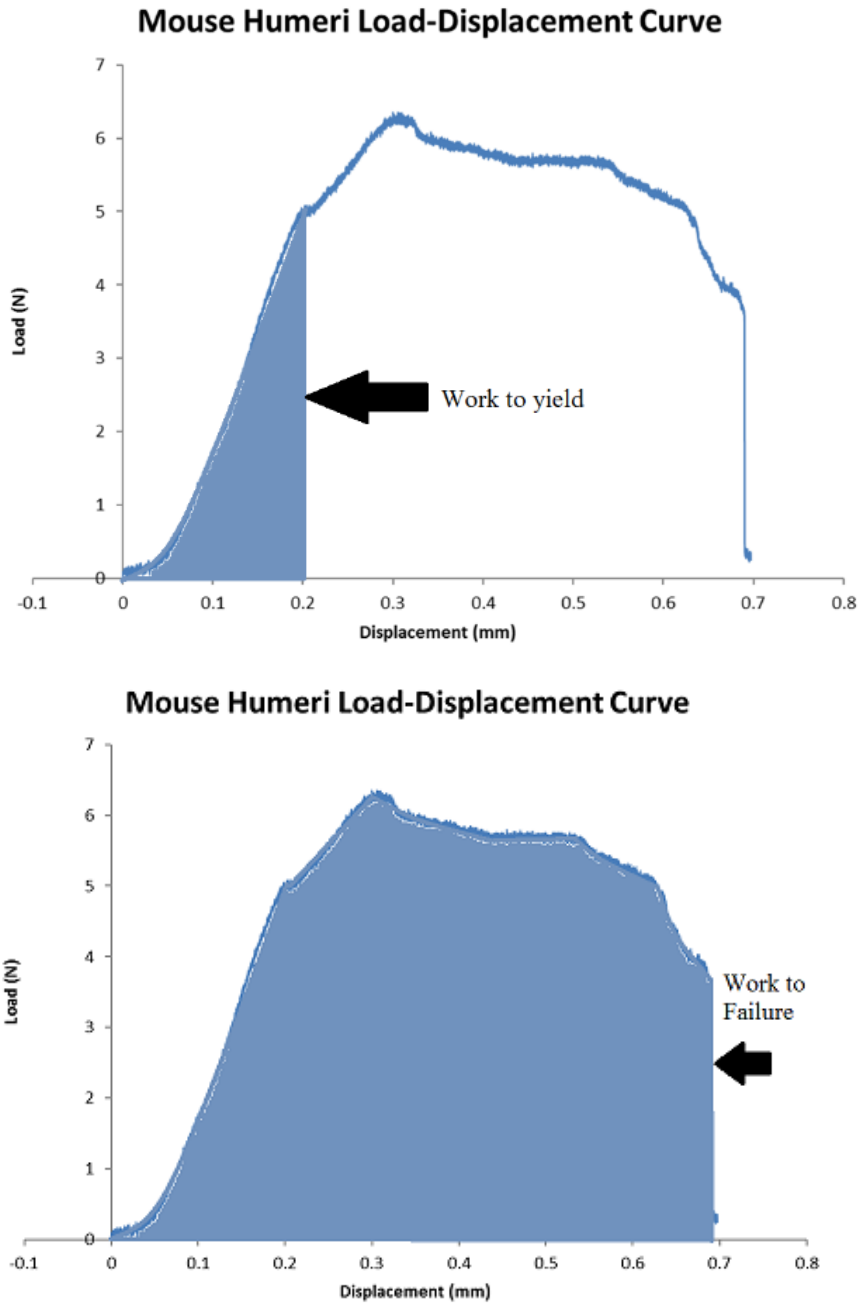

Figure 13. Representative figure of load-deformation curve for a mouse humeri displaying the area under the curve for calculating work to yield and work to fracture.

Recently, another method for characterizing bone toughness has been established. This method measures bone toughness with respect to resistance to crack initiation and propagation by obtaining crack growth resistance curves and the stress intensity factor, K_c, using notched 3-point bending mechanical testing (Ritchie et al., 2008).

Characterizing of Mechanical and Material Properties

Methods for evaluating bone mechanical and material properties at the macro-scale level include whole bone mechanical tests which involve loading the bone to failure by applying bending, tensile, compressive, or torsional stress. Bending stresses are typically induced in the bone by performing 3-point bending, notched 3-point bending, or 4-point bending mechanical tests, while tensile, compressive, and torsion tests are used to induce tensile, compressive, and torsional stresses, respectively. Furthermore, bulk tissue specimen tests such as microbeam testing and microindentation are used to evaluate the mechanical and material properties of the bone at the micro-scale level. Finally, nanoindentation is used to investigate the mechanical and material properties of the bone at the nano-scale level (Turner & Burr, 1993). In this thesis, bone strength and bone fracture toughness were examined at the macro-scale level as the mechanical properties of the whole bone were of primary interest. These properties were evaluated using 3-point bending, notched 3-point bending, and compressive mechanical testing.

Macro-Scale Mechanical Testing

The metrics for evaluating bone strength that were presented above may be obtained directly from load-deformation curves that are obtained from data points measured during mechanical testing (Figure 14).

The load-deformation curves can be converted to stress-strain curves to calculate the intrinsic material properties. Load-deformation curves for bones loaded typically exhibit a linear slope that is indicative of elastic deformation (Figure 13). In this region of the load-deformation curve, the bone matrix has been stretched but will return to its original dimensions if unloaded. Once the load on the bone exceeds a specific value, the curve ceases to be linear and begins to exhibit non-linear behavior. This portion of the curve has been traditionally characterized as the plastic region and indicates that the material is experiencing permanent deformation.

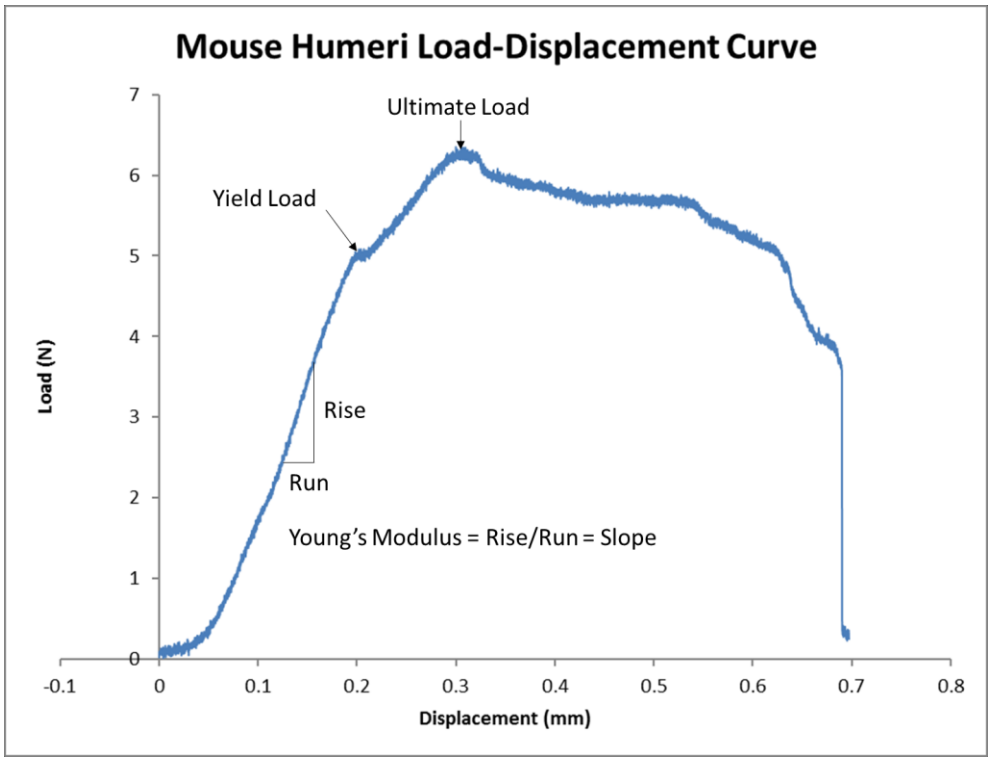

Figure 14. Representative load-deformation curve for a mouse humeri displaying the yield and ultimate load points as well as the method of calculating Young's modulus from the slope of the linear region of the curve.

The stiffness of bone indicates how resistant the bone is to elastic deformation and is represented numerically as the slope of the linear region of the load-deformation curve. This mechanical property correlates with the Young's Modulus material property, which is a factor of proportionality relating the stress to the strain of the bone (Turner & Burr, 1993).

The point at which the load-deformation curve of the bone transitions from linear to non-linear is defined as the yield load and represents the largest load that the bone can bear before it begins to experience permanent deformation. The corresponding point on the stress-strain curve is likewise termed the yield stress and is used as a measure of bone strength prior to permanent deformation. The maximum load or stress a bone can experience prior to fracture is referred to as the ultimate load or ultimate stress, respectively (Turner & Burr, 1993).

2.7.2.2 Geometric Properties

In addition to changes in composition, alterations in bone structure can result in differences in bone quality. Changes in cortical bone result from increases or decreases in bone porosity, cortical bone thickness, and alterations in the overall shape of the bone as characterized by measurements in the bone cross sectional area, moments of inertia along the major and minor axes, and the polar moment of inertia.

These changes can be assessed through several advanced imaging techniques which include scanning electron microscopy (SEM), optical microscopy, qualitative computed tomography (QCT), high-resolution magnetic resonance imaging (HR-MRI), micro-computed tomography (μCT), and synchrotron-computed tomography (SR-CT) (Turner & Burr,

1993). SEM and optical microscopy are used to image objects at the macro-scale level, while QCT, HR-MRI, and μCT can obtain images at the micro-scale level and SR-CT can capture images with nano-scale level resolution. In this thesis, SEM, μCT, and SR-CT were used to evaluate the geometric properties of bone.

Scanning Electron Microscopy

SEM was used to obtain high-resolution 2-D images of bone at the macro-scale level. This technology works by shooting a beam of electrons from a cathode through an electron lens that focuses the beam on the surface of a specimen and then analyzes the number of electrons that pass from the specimen to a collector. It then generates an image from that data which provides topographical and compositional information. There are several components of a scanning electron microscope. First, there is the source of the electrons, such as an electron gun containing a tungsten filament cathode, which emits a beam of electrons. Next, the electron beam travels down a column of electromagnetic lenses which condenses and focuses it. The beam then passes through deflection coils and a final lens aperture which directs the beam to a point on the sample surface. These deflection coils alter the direction of the beam to allow it to raster scan the surface of the sample. The beam then hits the sample. Finally, secondary electrons from molecules on the sample surface are released due to the energy exchange caused by the interaction of the electron beams. These electrons are collected by a specialized detector which measures the electromagnetic radiation and converts that information into a pixel value. Pixel values from each point scanned on the sample surface can then be reconstructed to generate an image (Oatley, Nixon, & Pease, 1966).

Micro-Computed Tomography

The second imaging technology that was used to assess bone morphology at the micro-scale level was micro-computed tomography

(μCT). μCT is a non-destructive imaging technique that uses x-ray attenuation data collected at multiple viewing angles to generate high-resolution 3-D images. μCT works by releasing micro-focused X-rays from a tube that passes through a collimator and a series of filters that narrow the energy spectrum to a desired range. Then, these x-rays are passed through the object being imaged and are collected in a 2-D charge-coupled device (CCD) array. That data is then sent to a computer which generates reconstructed images of the object that can be analyzed to assess structural properties. Recently, this technique has become the "gold standard" for evaluating bone microarchitecture *ex vivo (Bouxsein, 2005).* Several studies have evaluated the accuracy of geometric measurements obtained using 2-D and 3-D μCT scans in studies involving both animal and human specimens by comparing these measurements to those obtained using 2-D histomorphometric techniques (Barbier et al., 1999; Bonnet et al., 2009; Chappard, Retailleau-Gaborit, Legrand, Baslé, & Audran, 2005; Fanuscu & Chang, 2004; Kapadia et al., 1998; Kuhn, Goldstein, Feldkamp, Goulet, & Jesion, 1990). μCT offers several advantages over traditional histomorphometry in that it allows for direct 3-D imaging and assessment of trabecular morphology. The measurements obtained by μCT can evaluate much larger regions of interest more quickly than regular histomorphometry.

Synchrotron-Computed Tomography

The third technology used was SR-CT. ST-CT employs the same imaging modalities as μCT to obtain 2-D and 3-D scans of an object. The primary difference between these two imaging techniques is the resolution of the images that are obtained. The image resolution obtained using SR-CT is much greater than μCT. To obtain this increased resolution requires high powered, specially designed x-ray sources with highly sensitive array detectors. Very few laboratories possess the funds to purchase this

expensive equipment, so most studies involving SR-CT export their samples to specific external imaging facilities. For the second study in this thesis, bone samples were taken to a national synchrotron science facility, the Diamond Light Source in the UK, to be imaged.

2.7.2.3 Compositional Properties

Compositional properties of bone are used to evaluate how the collagen and mineral composition of the bone matrix changes and are thought to influence post-yield and ductile behavior of bone as well as bone mineral density (McCalden, McGeough, Barker, & Court-Brown, 1993). These properties consist of measurements of the changes in the type I collagen crosslinking primarily through modifications in the ratio of the number of pyridinoline and pyrrole (mature/irreducible) crosslinks to the number of ketoimine (immature/reducible) crosslinks present in the collagen, alterations in the collagen fiber orientation, changes in the density and crystallinity of hydroxyapatite minerals, and changes in the amounts of other elements present in the bone matrix composition.

Measurements of the trivalent to divalent collagen crosslinking ratios have correlated to bone tissue maturity, with the ratio increasing as ketoimine crosslinks are replaced by pyridinoline and pyrrole crosslinks through spontaneous biochemical processes as the collagen ages (Lynda Knott & Bailey, 1998). This is thought to influence bone strength, as studies osteoporotic avian bone have shown that decreases in pyrrole crosslinking correlates with decreased bone strength (L. Knott, Whitehead, Fleming, & Bailey, 1995).

Qualitative measurements of collagen fiber orientation determine how organized the bone matrix is at the compositional level. The orientation

of the collagen fibers has been shown to play a significant role on the amount of loading that a bone can bear, with increased strength exhibited in the direction of fiber orientation (Bakbak, Kayacan, & Akkuş, 2011).

The size, crystallinity, and composition of the hydroxyapatite crystals in the bone also have been shown to have a significant impact on bone strength. It has been demonstrated that increases in mineralization, or the mineral content of the bone, correlates to increases in the bone breaking stress as well as decreases in bone toughness (Currey, 1969). This indicates the hydroxyapatite crystals of the bone influence both bone strength and toughness.

Currently, there are several methods available for accessing these properties that include scanning electron microscopy (SEM), vibrational spectroscopy (Raman/Fourier transform infrared imaging), x-ray scattering techniques (SAXS/WAXD, nuclear magnetic resonance imaging (NMR), polarized light microscopy, gravimetric analyses, and chemical analyses of collagen crosslinking (Donnelly, 2011).

Fourier Transform Infrared Imaging

For this thesis, Fourier transform infrared imaging (FTIR-I) spectroscopy was used to evaluate the compositional properties of the bones that were examined. FTIR-I is an analytical technique that can be used to provide information about the molecular structure of various types of biological tissues. For this technique to work, a beam containing many frequencies of light is applied to the surface of a material. The surface of the material absorbs certain frequencies of light from the beam, depending on what molecular structures are present in the material. The molecular structures contain chemical bonds which vibrate at a certain frequency. When the light from the beam hits these bonds at that frequency, that light

gets absorbed by the material. Light that does not vibrate at the same frequency as the molecular structures in the material is transmitted through the material and measured by a detector. This measurement indicates how much energy is absorbed and at what frequencies. By applying Fourier transformations to these measurements, an absorbance spectrum can be generated and analyzed to see what frequencies were present in the material. Then, because these frequencies correspond to particular molecular structures, the spectra can be examined to quantitatively determine the type and amount of molecular structures that are present in the material.

The components of an FTIR-I spectrometer include an infrared (IR) source, detectors, a beam splitter, and a computer that can perform the Fourier transform and analyze the raw data. The materials used for an IR source depend on the wavelength range that is desired for the analysis. In general, there are three wavelength ranges: near-IR, mid-IR, and far-IR. The near-IR consists of shorter wavelengths, ranging from 10,000-4,000 cm^{-1}, and the typical IR source for this range is a tungsten-halogen lamp heated to about 1,200 K. For the mid-IR, the range consists of wavelengths ranging from 5,000-400 cm^{-1} and a heated silicon carbide element is typically used to generate the IR light. Finally, for far-IR, the wavelengths range from <400 cm^{-1} and typically require a mercury discharge lamp instead of a thermal source, especially for wavelengths < 200 cm^{-1} (Smith, Morgan, & Loewenstein, 1968). The next component is the detector which measures the IR radiation that is transmitted through the material by responding to changes in temperature caused by absorbing the IR radiation. These detectors are typically pyroelectric detectors for most applications, but can also be cooled photoelectric detectors for situations that require a high degree of sensitivity or quick response. The next component, a beam splitter, is used to increase the spectral IR range that can be examined using the FTIR-I spectrometer. For example, a beam splitter made from KBr with

a germanium based coating is used to absorb wavelengths beyond 400 cm^{-1}. A second beam splitter, made from Csl can be used additionally to extend that absorbance range to 200 cm^{-1}. The type of beam splitter and the number of beam splitters used is determined by the wavelength range desired for analysis. Finally, a computer that can process the data and apply the fast Fourier transform algorithm is the final component to a FTIR-I spectrometer and allows the user to obtain usable data for analysis.

2.8 Mouse Models

To gain a better understanding of the pathology of skeletal diseases and learn how to develop treatments, it is important to have disease models that can simulate the disease with a certain degree of accuracy while being readily available for a relatively low cost. For this reason, many scientific studies choose to develop mouse models which can simulate disease pathology for their research because of their mammalian physiology, low cost, rapid development, and high reproductivity.

Mice models which exhibit skeletal pathologies are developed by scientists through genetic engineering. A specific gene or set of genes which are related to the skeletal disease of interest are targeted and are either altered or inhibited. This generates transgenic or knock-out mice which are then inbred to create a strain of mice that over-express or under-express the genes that result in skeletal disease.

For this thesis, bones from three different mouse model types were tested using the bone characterization techniques described previously to examine the mechanical, material, geometric, and compositional bone properties at the macro-, micro-, and nano-scale levels. These mouse models included the C57BL/6 (WT) mouse, the tissue inhibitor of metalloproteinase-3 knock out *(Timp-3$^{-/-}$)* mouse, and the B6C3FE-

a/aCol1a2 (*oim*$^{-/-}$) mouse. A brief description of each mouse model is presented here:

C57BL/6

One of the most popular reference strains for genetic research is the C57BL/6 (WT) mouse model because it is one of the most genetically stable and best characterized inbred mouse models available (Pettitt et al., 2009). These mice models are also popular in studying skeletal diseases because of the similarities in bone physiology between mice and human skeletons (Jilka, 2013). As a result, this model is used to study normal age-related human bone physiology. Here, the C57BL/6 mouse model is used as a control to which the other mouse models are compared.

Tissue Inhibitor of Metalloproteinase-3

The *Timp-3*$^{-/-}$ mouse model is genetically modified so that the genes that encode tissue inhibitors of metalloproteinases-3 are suppressed. This prevents the mouse model from producing tissue inhibitors of metalloproteinases. This is thought to increase activity of matrix metalloproteinases (MMPs), a family of proteinases that play a role in tissue remodeling. Previously, this mouse model has been used to examine how alterations in remodeling affects the structural integrity of tissues (Leco et al., 2001). In this thesis, this mouse model will be used to examine how alterations in bone remodeling affect the bone properties at the marco-scale level by altering the geometric properties at the micro-scale level and the compositional properties at the nano-scale level.

Altered Collagen: Oim

Moderate to severe osteogenesis imperfecta is replicated in the B6C3FE-a/aCol1a2 (*oim*) mouse model. This model has been used extensively to evaluate the properties of bone affected by osteogenesis imperfecta and has helped scientists and researchers to develop treatments for the disease (A. Carriero, M. Doube, et al., 2014). It accurately replicates the molecular defects which compromise the bone tissue at the macro-scale. This mouse model will be used in this study to examine how bone structure changes between mice with osteogenesis imperfecta and those without the disease.

2.9 Bone Disease

Skeletal pathologies compromise overall bone health and decrease strength and toughness of the whole bone at the macro-scale level by altering the composition and structure of the bone at subservient levels of the bone hierarchy. For example, bone diseases caused by genetic mutations at the molecular level will create alterations in the processes of collagen formation and mineralization of hydroxyapatite crystals. These changes at the nano-scale level would alter the bone architecture at the micro-scale level. This changes how the bones responds to externally applied loads, resulting in changes in the mechanical and material properties of the bone, which can ultimately reduce bone strength and increase the risk of bone fracture. Skeletal pathologies caused by genetic abnormalities also may cause changes in the bone remodeling rate that could also contribute to decreases in bone strength by upsetting the balance between bone formation and resorption, a process that enables the bone to maintain proper material and structural integrity by replacing old, damaged bone with new bone (Unnanuntana, Rebolledo, Khair, DiCarlo, & Lane, 2011). By investigating the processes by which genetics influence bone quality and quantity, we can better understand how the bone mechanics is related to bone composition and structure at each of the different levels of the bone hierarchy. This

knowledge can then be utilized to improve treatments for patients with skeletal pathologies. In the following chapters, I investigate two skeletal pathologies which result from genetic alterations: TIMP-3 deficiency and OI, in order to learn how the bone changes in composition and structure at the nano-scale and mirco-scale levels in order to better understand why the bone mechanics change at the marco-scale level.

Chapter 3

The role of TIMP-3 on Bone Quality and Quantity

3.1 Tissue Inhibitor of Metalloproteinases-3 and Bone Extracellular Matrix

As mentioned previously, bone consists of a combination of living cells and an inanimate extracellular matrix (ECM). The ECM provides the bone with structure and organization and also serves as a scaffold that forms part of the cellular microenvironment that directs cell proliferation and differentiation (Alberts et al., 1997; Lukashev & Werb, 1998). Thus, the ECM is a crucial part of maintaining bone homeostasis (McCawley & Matrisian, 2001). In order to maintain structural integrity, the ECM continually undergoes a remodeling process where inveterate components of the ECM are either modified or degraded and replaced with new segments (Lu, Takai, Weaver, & Werb, 2011).

Matrix metalloproteinases (MMPs) are zinc-dependent endopeptidases that help regulate the processes of tissue remodeling in the ECM (Hijova, 2005; Varghese, 2006; Wojtowicz-Praga, Dickson, & Hawkins, 1997). This is thought to be accomplished primarily by proteolytic cleaving of the protein components of the ECM such as collagen, elastin, fibronectin, and laminin (Stamenkovic, 2003; Varghese, 2006; Watterson, 2013). The degradation of these protein components has been shown to initiate tissue remodeling in the ECM by facilitating cell motility by exposing cryptic promigratory sites in proteins such as laminin-5 and collagen type IV (Giannelli, Falk-Marzillier, Schiraldi, Stetler-

Stevenson, & Quaranta, 1997; J. Xu et al., 2001). Furthermore, the proteolytic cleaving of the protein components of the ECM has been shown to release cytokines and growth factors which aid in the remodeling process by stimulating cell activity and promoting new tissue formation (Manes et al., 1999; Suzuki, Raab, Moses, Fernandez, & Klagsbrun, 1997; Whitelock, Murdoch, Iozzo, & Underwood, 1996). In addition to direct ECM degradation, MMPs also indirectly influence the process of ECM remodeling by activating and inactivating growth factor precursors and cytokines through MMP-mediated cleavage (McCawley & Matrisian, 2001; McQuibban et al., 2001; Mu et al., 2002; Opdenakker, Van den Steen, & Van Damme, 2001; Yu & Stamenkovic, 2000). The process of remodeling the ECM is highly sensitive and needs to be carefully controlled, as excessive or uncontrolled remodeling of the ECM leads to abnormal cellular functioning that results in a variety of different pathological diseases (Bonnans, Chou, & Werb, 2014; Cox & Erler, 2011). Consequently, the amount of active MMPs in the body must be precisely regulated to ensure proper ECM homeostasis (Bonnans et al., 2014). This is accomplished through transcriptional control of MMP expression and through inhibition of MMP activity (Li & Li, 2013; Murphy et al., 1991; Nagase, Visse, & Murphy, 2006; Seccareccia et al., 2014; Visse & Nagase, 2003). MMP activity is inhibited primarily by either α2-macroglobulin or a family of proteins known collectively as tissue inhibitors of metalloproteinases (TIMPs) (Nagase et al., 2006). TIMP proteins are comprised of approximately 184 to 194 amino acids that can be subdivided into two domains: the N-terminal domain and the C-terminal domain (Nagase et al., 2006). The N-terminal domain consists of approximately 125 amino acids that enable the protein to bind to MMPs with a 1:1 molar stoichiometric ratio and prevent these proteinases from cleaving components of the ECM (Murphy et al., 1991; Visse & Nagase, 2003). There are currently four TIMPs (TIMP-1, -2, -3, and -4) that have been

identified in mammals (Brew, Dinakarpandian, & Nagase, 2000; Murphy, 2011; Qi et al., 2003). Studies have reported that each of the TIMPs can inhibit all MMPs that have currently been tested (Brew & Nagase, 2010; Nagase et al., 2006; Visse & Nagase, 2003). However, there are subtle differences between each of the TIMPs, as TIMP-1 has been shown to be less effective at inhibiting MT1-MMP, MT3-MMP, MT5-MMP, and MMP-19 while TIMP-2 and -3 are less effective at inhibiting MMP-3 and MMP-7 (Brew & Nagase, 2010; Hamze et al., 2007). Furthermore, TIMP-3 has also been shown to inhibit disintegrin and metalloproteases (ADAMs) (ADAM-10, -12, and -17) and disintegrin and metalloproteases with thrombospondin motifs (ADAMTSs) (ADAMTS-1, -4, and -5) (Nagase et al., 2006). These proteins are similar MMPs in that they are thought to play a role in tissue remodeling by cleaving proteins. ADAMs cleave the extracellular portions of transmembrane proteins while ADAMTSs cleave proteins like aggrecan, versican, brevican, and neurocan.

Due to their role in regulating MMP activity, TIMPs strongly influence ECM remodeling, and TIMP deficiency has been shown to result in variety of different diseases (Verstappen & Von den Hoff, 2006). In particular, many studies have been conducted to examine the impact that TIMP-3 deficiency has on *TIMP-3*$^{-/-}$ mice (Brew & Nagase, 2010).

As a result of increased ECM degradation, TIMP-3 deficiency was also shown to exacerbate the inflammatory process, (Mohammed et al., 2004) promote abnormal vascularization,(Janssen et al., 2008) increased bronchiole branching,(Gill et al., 2003) and increase susceptibility to arthritis (Sahebjam et al., 2007). In addition, TIMP-3 deficiency also resulted in increased pro-tumor necrosis factor-α (TNFα) as well as an increase in signaling between TNFα and transforming growth factor β1 (TGF-β1) due to unregulated ADAM17 activity (Brew & Nagase, 2010). The increased amount of TNFα resulted in accelerating the development of

dilated cardiomyopathy,(Kassiri et al., 2005) increased diabetic symptoms,(Federici et al., 2005) more aggressive cancer dissemination (Cruz-Munoz, Sanchez, et al., 2006) and increased tumor growth,(Cruz-Munoz, Kim, et al., 2006) and accelerated angiogenesis (Cruz-Munoz, Kim, et al., 2006). The increased cross-talk between TNFα and TGF-β1 resulted in excessive fibrosis (Kassiri et al., 2009). Thus, TIMP-3 deficiency has an impact on tissue remodeling, the development of disease, cancer progression, vascularization, inflammation, and innate immunity (Brew & Nagase, 2010). These results show that TIMP-3 deficiency is detrimental to tissue integrity and suggest that TIMP-3 may also have a direct impact on bone tissue.

Despite the body of research that has been conducted on the role of TIMP-3, it is still unknown how TIMP-3 influences bone integrity. Here, we reveal the influence of TIMP-3 on bone composition, structure and mechanics at a range of length scales. Specifically, we measure bone strength in compression and bending and toughness at the whole bone level. To explain differences in mechanical and material properties, we compare the morphology of the bone at the micro-scale length and determine the contribution of TIMP3 gene to the bone composition at the bone tissue level. Understanding how geometry, mechanical and material properties of cortical and trabecular bone change in *TIMP-3*$^{-/-}$ mice provides insights into the role of TIMP-3 in bone development and remodeling.

3.2 Materials and Methods

3.2.1 TIMP-3 Knock-out Mouse Model

To evaluate the effect of TIMP-3 deficiency on bone, a TIMP-3 knock out (*Timp-3*$^{-/-}$) mice model was generated by suppressing the TIMP-3 gene. This was accomplished by inserting probes of 1.8 kb *Timp*-3 cDNA into the genomic λ library from 129/Ola embryonic stem (ES) cells. 8 λ

clones were plated and plaque purified. Then PCR with *Pfu*I DNA polymerase was used to create two *Timp-3* gene fragments: a 723-bp "short arm" and a 6-kb "long arm". These arms were then subcloned into the pBS-neo vector such that the *Timp-3* gene was replaced by the Neo^R gene through the opposite transcriptional orientation. This vector was then introduced into the 129/Ola ES cells, which were then re-inserted into the mouse embryo (Leco et al., 2001). 6 wild type (WT) C57BL6 and 9 $Timp\text{-}3^{-/-}$ female mice were procured from a local colony and were raised following the Home Office (UK) guidelines for care and use of laboratory animals. The animals were euthanized at 8 weeks of age and stored at -20°C. The femurs, lumbar vertebrae (L5), caudal vertebrae (CA6), and humeri from each group of mice were dissected and cleaned of soft tissue.

Following dissection, a thin steel razor coated with 0.05 μm diamond suspension was used to remove the end plates and the posterior components of the L5 and CA6 vertebra to isolate the vertebral body. Once the vertebral bodies had been isolated, a Dremel tool was used to smooth the cranial and caudal ends of the vertebral bodies and make them flat and parallel. Then the vertebrae, along with the femurs and humeri, were wrapped in gauze, soaked in saline (Dulbecco's phosphate buffered saline solution 10x), and stored at -20°C to be maintained for micro-CT scanning, FTIR-I analysis, and mechanical testing.

3.2.2 Mechanical Properties of Bone Strength

3-point bending and compression mechanical tests were used to evaluate the mechanical and material properties of the WT and $Timp3^{-/-}$ humeri, and L5 vertebrae, respectively. An electromechanical test machine (Instron 5866) was used to perform each of the mechanical tests implemented in this study. All tests were conducted at room temperature, and the bone specimen were loaded at a rate of 1 μm/sec until failure. Measurements of both the load applied to the bone specimen during testing

and the displacement of the linear actuator applying the load to the bone specimen were measured and recorded using specialized software (Bluehill 2). An internally developed code (MATLAB R2015a) was used to evaluate the data and generate load-displacement and stress-strain curves from the raw data. The stiffness (N/mm), yield load (N), ultimate load (N), work to yield (mJ), work to fracture (mJ), Young's modulus (GPa), yield stress (MPa), and ultimate stress (MPa), were evaluated.

3.2.2.1 3-Point Bending Mechanical Testing

The mechanical and material properties of the WT and *Timp3*$^{-/-}$ humeri were evaluated by 3-point bending mechanical testing using an Instron 5866 mechanical testing machine with the testing configuration shown in Figure 1.

The humeri were positioned on the 3-point bending test mounts such that the medial-lateral axis of the bone was aligned perpendicularly to the direction of loading as shown in Figure 15, and the bone was oriented so that the anterior surface was in compression and the posterior surface was in tension during loading.

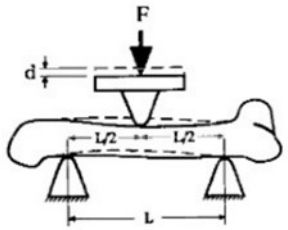

Figure 15. Schematic of the 3-point bending test of the long bone. L is the span length of the bone (mm), D is the displacement of the loading arm (mm), and F is the force applied to the bone from the loading arm (N).

The mounts were set apart by 6 mm to achieve the desired span length. Before testing, the lengths of the bone were measured using dial calipers, and the placement of the bones on the test rig were adjusted to ensure that the load was applied at the mid-shaft of each bone sample. Droplets of saline solution were applied to the humeri just prior to mechanical testing to ensure that the bones were hydrated. The humeri were then loaded to failure.

Load and displacement data were obtained directly from the mechanical testing and were used to determine the mechanical properties for the humeri. The stiffness of the material was determined by plotting the load-displacement curves and calculating the slope of the linear region of the curve. This was accomplished by selecting data points which marked the beginning and end of the linear region, respectively, and then calculating the change in the stress over the change in the strain. The yield load was calculated by plotting the 0.2% offset line and determining load corresponding with the point at which this line intersected with the load-displacement curve. The ultimate load was obtained by determining the largest value for the load data. The corresponding engineering stress and strain data were then calculated using the load and displacement data and the initial geometric measurements and the following formula for calculating the stress and strain for 3-point bending (Turner & Burr, 1993):

$$\sigma = \frac{FLc}{4I} \tag{2}$$

$$\varepsilon = \frac{12cd}{L^2} \tag{3}$$

Where σ is the stress (MPa), F is the applied load (N), L is the span length (mm), c is the average radius (mm) of the humeri from the cross-sectional centroid, I is the second moment of area about the mediolateral axis (mm^4), and d is the displacement (mm).

The material properties consisting of the Young's Modulus, Ultimate Stress, and Yield Stress for the humeri were obtained from the stress and strain data, the initial geometric measurements, and the following equations:

$$E = Stiffness \times \frac{L^3}{48I} \quad (4)$$

$$\sigma_{ult} = F_{ult} \times \frac{Lc}{4I} \quad (5)$$

$$\sigma_{yield} = F_{yield} \times \frac{Lc}{4I} \quad (6)$$

Where L is the span length (mm), I is the second moment of area about the mediolateral axis (mm^4), and c is the average radius (mm) of the humeri from the cross-sectional centroid.

3.2.2.2 Compression Test

The mechanical properties of the L5 vertebrae were evaluated using compression mechanical testing. The test was performed with the Instron 5866 testing machine using the testing configuration shown in Figure 16.

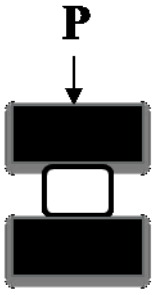

Figure 16. Schematic of compression mechanical testing of the short bone. P is the load applied to the bone from the compression plate.

The lengths of the L5 vertebrae were measured using digital Vernier calipers and then placed in the test rig with the long axis of the vertebral

body aligned parallel to the application of loading. The vertebrae were secured in the test rig with double sided tape that was applied to the bottom compression plate of the test rig to minimize movement during testing. Immediately before testing, the samples were hydrated with drops of saline solution. The stiffness, yield and ultimate load, and work to yield and work to fracture were determined from the load-displacement data recorded during testing.

3.2.2.3 Fracture Toughness

The fracture toughness of the WT and *Timp3*$^{-/-}$ femurs were evaluated by notched 3-point bending tests (Instron 5866). The femurs were placed on the mounts of the testing rig such that the medial-lateral axis of the bone was aligned perpendicularly to the direction of loading and the lengths were measured and used to determine how to position the bone so that the load would be applied at the mid-shaft length. The femurs were then marked and then notched on the posterior surface of the bone mid-shaft using a razor blade coated with 0.05 μm diamond suspension. The bones were placed in the testing rig such that the notch was oriented downwards in the direction of loading. The span length for the notched 3-point bending was determined to be 4 times the specimen width, or 5 mm, in accordance with the ASTM standards for single-edge-notch testing (ASTM Standard E399-09^{e2}). Each femur was hydrated with saline solution before testing. The femurs were then loaded to failure.

The load and displacement data were recorded as in the 3-point bending mechanical testing and the fracture toughness was evaluated using the "fracture instability method", which involved obtaining several measurements: the critical load at fracture instability, the crack angles (Notch and Instability angles), and the inner and outer radii of the femurs. The critical load at fracture instability was defined as the load value at failure and was measured during mechanical testing. The crack angles and

inner and outer radii of the femurs were evaluated from images of the cross-sectional fractured surfaces of each femur. These images were obtained using a scanning electron microscope with simultaneous back-scattering (INCA X-Act, Oxford Instruments) in low vacuum mode with a pressure of 30 Pa and a voltage level of 20kV. The geometric characteristics such as the centroid of the cross-sectional area, notch angle, instability angle, and mean inner and outer radii of the cortical shell were determined for each bone at the mid-diaphysis. All geometric values obtained were calculated from each image using an open-source image-processing program (ImageJ). The images were uploaded into the program as grayscale .tiff images that were then converted to a binary image using a threshold set manually in order to segment the cortical bone from the rest of the image. The binary image was then evaluated using ImageJ to determine the desired geometric properties for the humeri and L5 vertebrae. The centroid of each femur was calculated using a specialized plugin for the program (BoneJ plugin). The notch angle, instability angle, and mean inner and outer radii of the fractured femurs were evaluated manually using the appropriate tools within the imaging program.

These measurements were then used to calculate the stress intensity factor, K_c, using the following equation:

$$K_c = F_b \frac{SR_0 P_{inst}}{\pi(R_0^4 - R_i^4)} \sqrt{\pi \theta_{inst} R_{med}} \quad (7)$$

Where F_b is the geometrical factor in the K1 solution for an edge-cracked cylindrical pipe. S is the span length (m) between the supports used to hold the specimen in the testing machine. R_0, R_{med}, and R_i (m) are the outer, mean, and inner radii of the cortical bone, respectively. P_{inst} (N) is the break load. And Θ_{inst} (Radians) is the instability angle.

3.2.3 Bone Morphology

μCT scans were carried out on the humeri and CA6 vertebral bones. The collection and analysis of the results was carried out through a collaboration with Dr. Boskey at the Hospital for Special Surgery in New York. Scans were obtained using a Scanco μCT 35 system (Scanco Medical, Brüttisellen, Switzerland) with the following settings: 6 μm voxel size, 55 KVp, 0.36 degrees rotation step (180 degrees angular range) and 400 ms exposure per view. Scans were the reconstructed in 3-D using Scanco μCT software (HP, DECwindows Motif 1.6). Following reconstruction, a global threshold of 0.4 g/c was used to segment the volumes of the reconstructed 3-D images and then total volume (TV), bone volume (BV), bone volume density (BV/TV) porosity (Ct.Po = pore volume/TV), cortical area fraction (Ct.AR/Tt.Ar), mean cortical thickness (Ct.Th), the second moments of inertia along the major and minor axis (I_{max} and I_{min}), the polar moment of inertia (J), tissue mineral density (TMD) and bone mass (TMD/Ct.Po) of the cortical bone were analyzed (Bouxsein et al., 2010). BV, TV, BV/TV, and TMD of the trabecular bone were also analyzed in addition to the connectivity density (Conn-D), trabecular number (Tb.N), trabecular thickness (Tb.Th), and trabecular spacing (Tb.Sp) (Bouxsein et al., 2010).

3.2.4 Bone Composition

FTIRI-spectroscopy was used to measure changes in the chemical composition and distribution of the organic and inorganic components of the WT and *Timp-3*$^{-/-}$ mice bone. The right femurs from each mouse were sent to Dr. Boskey for evaluation. Prior to scanning, the femurs were fixed in 905 ethanol and embedded in polymethylmethacrylate (PMMA). Scans were obtained using a Perkin Elmer Spotlight Imaging system with a 4 cm^{-1} spectral resolution and a 6.25 μm spatial resolution. Each bone was scanned in 2 μm thick sections to obtain 5 images from the cortical bone of the

femur and 5 images from the trabecular bone. A specialized software (ISYS, Spectral Dimensions, Olney, MD) was then used to process the scans. Interference from the atmospheric H_2O and the CO_2 was subtracted from the captured spectra and normalized using a linear baseline. For this study, five compositional parameters were examined: the mineral-to-matrix ratio, the carbonate-to-phosphate ratio, the mature-to-immature collagen enzymatic crosslinking ratio, the mineral crystallinity, and the acid phosphate substitution. These parameters were obtained by evaluating the wave intensities for the spectra obtained during scanning. The mineral to matrix ratio was calculated as the ratio of the area of the 900 – 1,200 cm^{-1} phosphate band to the area of the 1,520-1,720 cm^{-1} amide I and amide II band. The carbonate-to-phosphate ratio was defined as the area of the 850-890 cm^{-1} carbonate band to the 1,520-1,720 cm^{-1} amide I and amide II band. The mature-to-immature collagen enzymatic crosslinking ratio was defined as the ratio of the relative intensity values of the peaks of the 1,660 cm^{-1}/1,690 cm^{-1} subbands to the relative intensity values of the peaks of the amide I and amide II 1,520-1,720 cm^{-1} subbands. The crystallinity was defined as the intensity ratio of the subbands at 1,030 and 1,020 cm^{-1}. Finally, the acid phosphate content was measured by evaluating the intensity ratios of the 1,028 and 1,096 cm^{-1} sub-bands. The heterogeneity of these parameters was also analyzed.

3.2.5 Statistical Analysis

A specialized statistical software package (SPSS, IBM, Somers, NY) was used to analyze the data obtained from the mechanical, geometric, and compositional results and determine which of the measured parameters where statistically different between the *Timp-3*$^{-/-}$ and WT mice bone. First, the Shapiro-Wilk test and the Levene's test were used to evaluate the normal distribution and homogeneity of variance of the data for each

mechanical, material, and morphological parameter investigated by mechanically testing the humeri and the L5 vertebrae as well as the morphologically examined through μCT analysis of the humeri and CA6 vertebrae. If the data for each variable was considered to have a normal distribution and could be considered homogeneous, then the Student's independent *t*-test was used to evaluate statistical significance between groups. If the data failed the Shapiro-Wilk test, it was not normally distributed, and a non-parametric test known as the Mann-Whitney rank test was then used to determine statistically significant differences between groups. For the compositional parameters investigated using FTIR analysis, statistical significance was evaluated using analysis of variance (one-way nested ANOVA). For each test, parameters with calculated p-value that were less than 0.05 were statistically significant.

3.3 Results

3.3.1 Mechanics of *TIMP-3*$^{-/-}$ Bone

The data obtained from the 3-point bending and compression mechanical testing indicated that the values for the yield and ultimate load, work to yield, and yield and ultimate stress obtained for both the humeri and L5 vertebrae from the *Timp-3*$^{-/-}$ mice were significantly lower than those obtained for the WT mice. Individually, the stiffness of the *Timp-3*$^{-/-}$ humeri and the work to fracture of the *Timp-3*$^{-/-}$ L5 vertebrae were also significantly reduced, while neither type of bone revealed significant differences in the elastic modulus. The results from the notched 3-point bending mechanical testing performed on the femurs indicated that the fracture toughness of the *Timp-3*$^{-/-}$ mice was significantly reduced when compared to their WT counterparts. This data is summarized in Tables 1, 2, and 3.

Mechanical Parameter	Humeri		
	WT (N=6)	TIMP-3$^{-/-}$ (N=9)	p-value
Stiffness (N/mm)	94.32 ± 11.10	43.85 ± 13.73	<0.001
Yield Load (N)	10.40 ± 2.05	4.50 ± 1.28	<0.001
Ultimate Load (N)	13.33 ± 1.52	6.42 ± 1.39	<0.001
Work to Yield (mJ)	0.65 ± 0.25	0.25 ± 0.10	<0.001
Work to Fracture (mJ)	2.65 ± 0.67	2.20 ± 0.99	N.S.
Elastic Modulus (GPa)	8.66 ± 1.55	6.60 ± 2.69	N.S.
Yield Stress (MPa)	102.80 ± 12.20	59.85 ± 15.84	<0.001
Ultimate Stress (MPa)	133.12 ± 15.37	86.48 ± 19.35	<0.001

Table 1. Mechanical and material properties obtained for the humeri of the WT and Timp-3$^{-/-}$ cortical mouse bone obtained from 3-point bending. These results show that the stiffness, yield and ultimate load, the work to yield, and yield and ultimate stress are significantly lower in the Timp-3$^{-/-}$ humeri compared to the WT counterparts. The values for Young's modulus for the humeri were not significantly different, but this was due to the high variation within the groups.

Mechanical Parameter	L5 Vertebrae		
	WT (N=6)	TIMP-3$^{-/-}$ (N=9)	p-value
Stiffness (N/mm)	90.28 ± 34.08	63.78 ± 31.94	N.S.
Yield Load (N)	10.35 ± 2.37	5.36 ± 2.56	<0.01
Ultimate Load (N)	12.92 ± 2.50	6.39 ± 3.04	<0.01
Work to Yield (mJ)	0.70 ± 0.32	0.27 ± 0.19	<0.01
Elastic Modulus (GPa)	0.11 ± 0.07	0.07 ± 0.03	N.S.
Yield Stress (MPa)	4.67 ± 1.42	2.52 ± 1.20	<0.01
Ultimate Stress (MPa)	5.93 ± 1.42	3.00 ± 1.41	<0.01

Table 2. Mechanical and material properties obtained for the L5 vertebrae of the WT and Timp-3$^{-/-}$ cortical mouse bone obtained from compression testing. These results show that the stiffness, yield and ultimate load, the work to yield, and yield and ultimate stress are significantly lower in the Timp-3$^{-/-}$ L5 vertebrae compared to the WT counterparts. The values for Young's modulus for the vertebrae were not significantly different, but this was due to the high variation within the groups.

Mechanical Parameter	Femurs		
	WT (N=6)	TIMP-3$^{-/-}$ (N=9)	p-value
Fracture Toughness (MPa√m)	6.36 ± 0.68	4.28 ± 0.31	<0.01

Table 3. Fracture toughness measurements in terms of the stress intensity factor, K_c, obtained for the femurs of the WT and Timp-3$^{-/-}$ cortical mouse bone were evaluated using notched 3-point bending. These results show that the fracture toughness is significantly lower in the Timp-3$^{-/-}$ humeri compared to the WT counterparts.

3.3.2 Architecture of *Timp-3*$^{-/-}$ Bone

The μCT analysis revealed that the microarchitecture of *Timp-3*$^{-/-}$ cortical bone in the humeri and L5 vertebrae and the trabecular bone of the humeri was significantly altered from the microarchitecture found in normal WT mice. The cortical bone was found to be smaller, thinner, had a different morphology, and was more porous, as indicated by significantly reduced TV, BV, BV/TV, Ct.Ar/Tt.Ar, Ct.Th, I_{max}, I_{min}, and J values and significantly increased Ct.Po. The trabecular bone was found to be more numerous and dense, with greater interconnectivity, but thinner and more tightly packed together, as indicated by significantly lower TV, Tb.Th, and Tb.Sp values and significantly higher BV/TV, Conn-D, and Tb.N values. These values are reported in Tables 4, 5, and 6.

μCT Index	Humeri Cortical Bone		
	WT (N=6)	TIMP-3$^{-/-}$ (N=9)	p-value
TV (mm^3)	1.41±0.08	1.11±0.07	<0.001
BV (mm^3)	0.83±0.04	0.6±0.04	<0.001
BV/TV (%)	59±1	54±2	<0.001
Ct.Po (%)	5.04±1.42	8.51±0.51	<0.01
Ct.Ar/Tt.Ar (%)	59±1	54±2	<0.001
TRI-Ct.Th (mm)	0.20±0.00	0.15±0.01	<0.001
Imax (mm^4)	0.09±0.01	0.05±0.07	<0.001
Imin (mm^4)	0.06±0.01	0.03±0.01	<0.001
J (mm^4)	0.14±0.01	0.08±0.01	<0.001
TMD (mg/cm^{-3})	1124.91±4.83	1063.95±16.41	<0.001
Bone Mass (mg)	236.50±56.35	125.35±7.83	<0.01

Table 4. Geometric properties of the humeri cortical bone for both the WT and Timp-3$^{-/-}$ mice. The values of the total volume, bone volume, bone volume density, thickness, cross sectional area, moments of inertia, tissue mineral density, and overall bone mass were significantly lower for the Timp-3$^{-/-}$ mice. The Timp-3$^{-/-}$ mice also exhibited higher cortical porosity compared to their WT counterparts.

μCT Index	Vertebrae Cortical Bone		
	WT (N=6)	TIMP-3$^{-/-}$ (N=9)	p-value
TV (mm^3)	1.20±0.11	1.01±0.09	<0.05
BV (mm^3)	0.79±0.06	0.56±0.04	<0.001
BV/TV (%)	66±2	56±3	<0.001
Ct.Po (%)	7±1	16±5	<0.01
Ct.Ar/Tt.Ar (%)	66±2	56±3	<0.001
TRI-Ct.Th (mm)	0.18±0.01	0.11±0.02	<0.01
Imax (mm^4)	0.13±0.03	0.09±0.02	<0.01
Imin (mm^4)	0.12±0.02	0.07±0.01	<0.001
J (mm^4)	0.26±0.05	0.16±0.03	<0.01
TMD (mg/cm^{-3})	938.49±12.62	892.49±72.33	N.S.
Bone Mass (mg)	132.48±12.07	62.08±25.64	<0.001

Table 5. Geometric properties of the CA6 vertebrae cortical bone for both the WT and Timp-3$^{-/-}$ mice. The values of the total volume, bone volume, bone volume density, thickness, cross sectional area, moments of inertia, and overall bone mass were significantly lower for the Timp-3$^{-/-}$ mice. The Timp-3$^{-/-}$ mice also exhibited higher cortical porosity compared to their WT counterparts.

μCT Index	Humeri Trabecular Bone		
	WT (N=6)	TIMP-3$^{-/-}$ (N=9)	p-value
TV (mm^3)	1.57±0.05	1.16±0.18	<0.001
BV (mm^3)	0.19±0.02	0.16±0.03	N.S.
BV/TV (%)	12±1	14±1	<0.05
Conn-Dens. (mm^{-3})	294.13±38.84	552.83±113.67	<0.001
Tb.N (1/mm)	4.47±0.32	6.15±0.67	<0.001
Tb.Th (mm)	0.04±0.00	0.03±0.00	<0.001
Tb.Sp (mm)	0.23±0.02	0.16±0.02	<0.001
TMD (mm^{-3})	914.41±8.24	873.81±18.99	<0.01

Table 6. Geometric properties of the humeri trabecular bone for both the WT and Timp-3$^{-/-}$ mice. The values of the bone volume density, connectivity density, and trabecular number were significantly higher and the total volume, trabecular thickness, trabecular spacing, and tissue mineral density were significantly lower for the Timp-3$^{-/-}$ mice.

3.3.3 Composition of *Timp-3*$^{-/-}$ Bone

A comparison of the chemical composition between the *Timp-3*$^{-/-}$ and WT bones using FTIR analysis indicated that there was less carbonate and more acid phosphate in the TIMP-3 deficient cortical and trabecular bone. The *Timp-3*$^{-/-}$ trabecular bone also had an increased collagen enzymatic crosslinking ratio. Mapping of the surface of the *Timp-3*$^{-/-}$ and WT bones revealed that the heterogeneity of the collagen crosslinking ratio was increased in the *Timp-3*$^{-/-}$ cortical and trabecular bone. The trabecular bone also exhibited a decrease in the heterogeneity of the carbonate-to-phosphate ratio and an increase in the heterogeneity of the mineral crystallinity. The data from this analysis is summarized in Tables 7 and 8.

FTIR Index	Cortical Bone		
	WT (N=6)	TIMP-3$^{-/-}$ (N=9)	p-value
Mineral/Matrix Ratio	6.66 ± 0.56	6.97 ± 0.89	N.S.
Carbonate/Phosphate Ratio (10^{-3})	6.20 ± 0.50	5.50 ± 0.80	<0.05
Crosslink Ratio	3.77 ± 0.13	3.87 ± 0.19	N.S.
Crystallinity	1.20 ± 0.03	1.20 ± 0.04	N.S.
Acid Phosphate	0.49 ±0.02	0.52 ± 0.05	<0.05
M/M Heterogeneity	2.14 ± 0.59	2.27 ± 0.61	N.S.
C/P Heterogeneity	0.002 ± 0.000	0.002 ± 0.000	N.S.
C/P Heterogeneity (10^{-3})	2.10 ± 0.1	2.20 ± 0.20	<0.01
Crystallinity Heterogeneity (10^{-2})	12.97 ± 1.53	12.42 ± 2.05	N.S.

Table 7. Results of the FTIR analysis for the cortical bone from the WT and Timp-3$^{-/-}$ femurs. The analysis of the results revealed that there was an increase in the acid phosphate content and the heterogeneity of the mature-to-immature collagen crosslinking ratio and a decrease in the carbonate substitution of the hydroxyapatite crystals for the cortical bone.

FTIR Index	Trabecular Bone		
	WT (N=6)	TIMP-3$^{-/-}$ (N=9)	p-value
Mineral/Matrix Ratio	5.57 ± 0.45	5.87 ± 0.41	N.S.
Carbonate/Phosphate Ratio (10^{-3})	5.90 ± 0.80	4.30 ± 0.50	<0.001
Crosslink Ratio	3.96 ± 0.20	4.35 ± 0.24	<0.01
Crystallinity	1.15 ± 0.02	1.16 ± 0.03	N.S.
Acid Phosphate	0.63 ± 0.04	0.71 ± 0.05	<0.01
M/M Heterogeneity	2.51 ± 0.49	2.81 ± 0.65	N.S.
C/P Heterogeneity (10^{-3})	2.60 ± 0.30	3.30 ± 0.40	<0.001
Crosslink Heterogeneity	0.50 ± 0.08	0.85 ± 0.30	<0.05
Crystallinity Heterogeneity (10^{-2})	19.07 ± 1.71	16.72 ± 0.81	<0.01

Table 8. Results of the FTIR analysis for the trabecular bone from the WT and *Timp-3*$^{-/-}$ femurs. The analysis of the results revealed that there was an increase in the acid phosphate content and the heterogeneity of the mature-to-immature collagen crosslinking ratio and a decrease in the carbonate substitution of the hydroxyapatite crystals for the cortical bone.

3.4 Discussion

In this study, the geometric, compositional, mechanical, and material properties of healthy bone and bone with a TIMP-3 deficiency were evaluated to investigate the impact of TIMP-3 on bone health. The results from this study revealed that TIMP-3 deficiency does indeed have a

significant impact on the structure, composition, and mechanics of bone and is important to understand in order to better assess bone health and to produce more effective clinical treatments for bone diseases.

The results from the mechanical tests performed on the humeri, L5 vertebrae and femurs showed that the *Timp-3*$^{-/-}$ mice had either similar or significantly reduced mechanical properties when compared to their WT counterparts, demonstrating that a lack of TIMP-3 adversely affects bone mechanical properties. This result is not surprising, as several previous studies found that TIMP-3 deficiency resulted in compromised tissue quality and function (Hammoud, Lu, Lei, & Feng, 2011; Javaheri et al., 2016; Leco et al., 2001; Erica L. Martin et al., 2007; Mohammed et al., 2004; Murthy et al., 2012). More specifically, both the long bones (humeri and femurs) and the short bones (L5 vertebrae) demonstrated significant reductions in the yield and ultimate load bearing capabilities, as well as lower yield and ultimate stress values and reduction in the work to yield. The long bones also had significant reductions in the stiffness of the bones as well as fracture toughness. In addition, the elastic modulus was reduced in the *Timp-3*$^{-/-}$ bone, but the results did not turn out to be statistically significant due to high variation within the sample size analyzed. Bone strength is a function of bone quality and quantity (Donnelly, 2011). Therefore, the observed reductions in bone mechanical and material properties may be explained as a result of alterations in bone structure and composition as well as the overall bone mass. The results from our morphological and compositional analyses suggest that this hypothesis is correct. The data from the μCT analysis revealed that TIMP-3 deficiency changes both the structure of the cortical and trabecular bones. The *Timp-3*$^{-/-}$ cortical bones were smaller, as indicated by the reduced cross-sectional area and volume, had altered geometry, as indicated by the changes in the moments of inertia, were thinner, and were more porous. The amount of

overall cortical bone also decreased, as the bone mass was found to be significantly reduced. One possible explanation for the increased cortical bone porosity is that there was an increase in blood vessel formation, or angiogenesis, in these bones, due to the excessive activity of MMPs caused by the lack of TIMP-3. One MMP in particular, MMP-9, has been identified as a stimulator for angiogenesis in the bone and may be the reason for the increased cortical porosity observed in this study (Bruni-Cardoso, Johnson, Vessella, Peterson, & Lynch, 2010). This high porosity would explain why the *Timp-3*$^{-/-}$ femurs exhibited reduced fracture toughness, as previous studies have found that high porosity increases the number of high stress concentration areas within the bone (Alessandra Carriero et al., 2014) and results in increased crack propagation velocity (Carriero, Zimmermann, Shefelbine, & Ritchie, 2014), both of which led to reduced resistance to fracture in bone (Ural & Vashishth, 2007). Another explanation for the increased porosity as well as the decreased cortical thickness is that the rate of bone remodeling in *Timp-3*$^{-/-}$ bone is significantly altered. Previous studies have shown that increased porosity and cortical thinning correlates with increased bone remodeling (Bell, Loveridge, Power, Rushton, & Reeve, 1999; Power et al., 2003; Shigdel et al., 2015). In support of this, one recent study demonstrated that TIMP-3 deficiency resulted in an increased number of osteoclasts, but not osteoblasts, suggesting that there was an increase in the amount of bone resorption, but not bone formation in the *Timp-3*$^{-/-}$ bone (Javaheri et al., 2016). Since MMPs, ADAMs, and ADAMTSs are involved in bone remodeling by breaking down the ECM into collagen fragments which stimulate osteoclast activity, it is possible that TIMP-3 deficiency indirectly increases bone remodeling by failing to inhibit any excessive metalloproteinase activity. The hypothesis that the changes in the microstructure of the bone were due to alterations in the bone remodeling is further supported by the changes in composition indicated by the results of the FTIR analysis. The decreased carbonate-to-phosphate

ratio, increase in acid phosphate, and increased heterogeneity of the mature-to-immature enzymatic collagen crosslinking ratio all suggest that there is increased remodeling in the *Timp-3*$^{-/-}$ bone. This is because previous studies which investigated carbonate content in bone found that carbonate substitutions in the crystals increase as the bone matures, suggesting that less carbonate means that the bone is less mature, as it has not had the time to substitute the carbonate into the bone mineral (Ou-Yang, Paschalis, Mayo, Boskey, & Mendelsohn, 2001). The increased acid phosphate content also indicates that the bone is less mature, as acid phosphate is found in areas of new bone formation and mineral deposition (Spevak, Flach, Hunter, Mendelsohn, & Boskey, 2013). Increases in the heterogeneity of the collagen crosslinking ratio has also been found to indicate increased bone remodeling (Donnelly et al., 2012).

The results from the FTIR analysis of the *Timp-3*$^{-/-}$ trabecular bone also suggested an increase in bone remodelling. Like the cortical bone, the *Timp-3*$^{-/-}$ trabecular bone exhibited signs of increased bone remodelling. The results obtained in this study demonstrated decreases in the carbonate-to-phosphate ratio and increases in the acid phosphate content The results also validated the heterogeneity of the mature-to-immature enzymatic collagen crosslinking ratio, as well as increases in the heterogeneity of the carbonate-to-phosphate ratio and mineral crystallinity (Donnelly et al., 2012; Gourion-Arsiquaud et al., 2013).

These findings indicate that TIMP-3 deficiency impacts bone at the nanoscale level by altering the composition of the bone, which in turn, creates changes in the architecture of the bone at the microscale level. This ultimately cause reductions in the mechanical and material properties at the macroscale level. While the exact pathway by which TIMP-3 influences bone remodeling was not determined conclusively, results from previous

studies provide some insight into exactly how TIMP-3 deficiency could alter metalloproteinase activity and ultimately increase bone remodeling. For example, several studies examined the effects of increased MMP-1, -2, -8, -9, -13, and -14 activity on bone and found increases in bone remodeling due to increased collage degradation (Garnero et al., 2003; Holmbeck et al., 1999; Inada et al., 2004; E. L. Martin et al., 2005; Ohuchi et al., 1997). Additionally, researchers have suggested that ADAMs and ADAMTSs could play a role in bone remodeling by stimulating osteoblast and osteoclast activity (Botter et al., 2009; Marzia et al., 2011; Verrier, Hogan, McKie, & Horton, 2004). Specifically, ADAM-10 and ADAM-12 were found to play a role in directing human peripheral blood mononuclear cells to differentiate into osteoblasts and osteoclasts, (Verrier et al., 2004) while ADAM-15 was found to increase osteoblast activity (Marzia et al., 2011). Thus, it is possible that by inhibiting any of these MMPs, ADAMs, and ADAMTSs, TIMP-3 indirectly increases bone remodeling; however, future studies would need to evaluate the levels of these proteinases to determine whether they are elevated due to TIMP-3 deficiency and would have to show that this increased metalloproteinase activity correlated with increased bone remodeling.

3.5 Conclusions

The results of this research show that TIMP-3 plays a crucial role in maintaining bone quality and quantity, as TIMP-3 deficiency was shown to result in reduced mechanical and material properties as a result of altered bone structure and composition. Specifically, the decreases in yield and ultimate load, work to yield, yield and ultimate stress, and fracture toughness appeared to be the result of reductions in cortical bone thickness, increased cortical porosity, and decreases in the overall bone mass as well as decreases in hydroxyapatite crystal size and orientation. These changes in bone microarchitecture and composition appear to be the result of increased

bone remodeling, a hypothesis that is supported by the observed reductions in the carbonate-to-phosphate ratio, the increased acid phosphate content, and the increased heterogeneity of the cortical and trabecular bones. It is proposed that this increase in bone remodeling is the result of increased MMP, ADAM, and ADAMTS activity due to the lack of TIMP-3. Thus, this study found that TIMP-3 helps to maintain bone quality and quantity by regulating bone remodeling and enabling the bone ECM to mature. This allows the bone to fully develop and obtain optimal compositional, structural, mechanical, and material properties. Future research can use this data to further investigate how TIMP-3 influences MMP, ADAM, and ADAMTS activity, and how it indirectly alters bone properties. This knowledge can help clinicians and researchers develop novel medicines and therapies that can be used to treat diseases involving altered TIMP-3, MMP, ADAM, and ADAMTS activity.

Chapter 4

Altered Cortical Porosity and Structure in Osteogenesis Imperfecta Cochlea Bone

4.1 Introduction

Osteogenesis Imperfecta (OI) is a hereditary connective tissue disorder which results from mutations in the genes responsible for the formation of type I collagen (COL1) (Huber, 2007; Pillion, Vernick, & Shapiro, 2011). It is a major genetic bone disease with an incidence of 1 in 15,000 child births (Byers & Cole, 2002; Huber, 2007; Millington-Ward, McMahon, & Farrar, 2005; Niyibizi, Wang, Mi, & Robbins, 2004). One study stated that approximately 25,000 individuals in the United States alone live with this condition; however, it is believed that the real incidence is much higher than that because of the vast number of people with mild OI who are never officially diagnosed with the disease (Pillion et al., 2011).

OI is primarily characterized by an increase in bone fragility and skeletal deformities, however, other typical manifestations include dentinogenesis imperfecta (brittle teeth), blue sclera, increased susceptibility to bruising, joint laxity, and hearing loss (Niyibizi et al., 2004; Pillion et al., 2011; Rauch & Glorieux, 2004). These symptoms are the result of defects in tissues containing collagen such as bone, tendons, ligaments, skin, sclera, teeth, and middle and inner ear, with the major manifestation being brittle bone (Huber, 2007). OI currently manifests itself as 1 of 17 different clinically recognized phenotypes that are classified based on the symptoms and the source of the genetic mutations which cause alterations in connective tissue. Of these 17 phenotypes, there are 4 that are

primarily responsible for mutations in the type I collagen that results in OI. These primary phenotypes are summarized below in Table 9.

Type	Inheritance	Clinical	Incidence
I	AD	Mild, blue sclerae, fractures with little or no deformity, hearing loss, dentinogenesis imperfecta (DI)	60%
II	AD, AR	Lethal, pulmonary insufficiency, beaded ribs, rhizomelic hearing loss	10%
III	AD, AR	Progressive deforming intrauterine fractures, deformed limbs, scoliosis, white or blue sclerae hearing loss, DI	10%
IV	AD	Moderately severe, limb deformity, sclerae blue early and lighten with age, scoliosis	15%

Table 9. Primary phenotypes of osteogenesis imperfecta phenotypes (AD = autosomal dominant, AR = autosomal recessive.) (Pillion & Shapiro, 2008)..

Mutations in the COL1A1 and COL1A2 cause approximately 95% of the OI cases. COL1A1 and COL1A2 are primarily responsible for the synthesis of the proalpha-1 and proalpha-2 polypeptide chains which bind together to form a triple helical structure known as type I collagen. Mutations in these genes adversely affect the type I collagen fiber, which results in compromised connective tissue in multiple organs throughout the

body ranging from bone, to the sclerae in the eye, to vascular structures in the mitral and aortic valves, to the auditory structures in the ear. The symptoms that result from these mutations can range from mild, to severe and lethal, depending on how the COL1A1 and COL1A2 genes are altered. Mutations which inhibit one allele of the COL1A1 gene result in the milder forms of OI, while dominant negative mutations in COL1A1 or COL1A2 cause the severe or lethal forms of OI (Gajko-Galicka, 2002). The mutations which inhibit one allele of the COL1A1 gene are known as "excluded" mutations because these mutations result in the exclusion of product from the mutant allele from the mature collagen molecule. This means that only half of the normal amount of type 1 collagen gets produced. However, the structure of the type 1 collagen does not change because of the mutation. The other mutations which affect both the COL1A1 and COL1A2 genes are called "inclusive" mutations because these mutations produce altered proα1 and proα2 chains to be incorporated into the type I collagen triple helix. The abnormal type I collagen chains are structurally compromised because of changes in the amino acids which comprise the type 1 collagen fibers. Normally, type 1 collagen is formed from a chain of the following repeated amino acid sequence: G-X-Y, where G is glycine, X is usually proline and Y is typically hydroxyproline. However, in cases of "inclusive" or dominant negative mutations, the glycine is substituted for other amino acids which results in improper folding of the proα chains in the helical structure, making the structure less stable than normal and compromising the connective tissue by altering the fiber structure and providing an abnormal template for mineralization (Baker, Ramshaw, Chan, Cole, & Bateman, 1989; W. G. Cole, 1998; William G. Cole, 2002).

As mentioned previously, hearing loss is a prominent symptom of OI; however, the exact prevalence of hearing loss remains uncertain. Several studies have stated that of the patients diagnosed with OI,

approximately half suffer from some form of hearing loss (Kuurila, Johansson, Kaitila, & GrêNman, 2002; Stewart & O'Reilly, 1989). In reality, the actual number of patients with impaired hearing loss is most likely much greater, as other studies have reported that the prevalence of hearing loss is as high as approximately 65 – 72% (Stewart & O'Reilly, 1989). However, differences in these reported results are most likely due to differences in the definitions used to quantify hearing loss (Imani, Vijayasekaran, & Lannigan, 2003).

OI-related hearing loss is classified as either conductive, sensorineural, or mixed, depending on the cause of hearing loss. Broadly speaking, conductive hearing loss refers to cases where hearing loss results from failure to properly transmit sound waves from the outer ear through the tympanic membrane to the middle ear and then into the cochlea. However, an exact definition remains elusive, as different studies have not agreed on one common term. For example, one study by Riedner et al., held that hearing loss in the air-bone gap was 5 dB or greater at two or more octave frequencies ranging from 500 to 4,000 Hz, while Shapiro et al., stated that the hearing loss in the air-bone gap needed to be at least 15 dB at one or more octave frequencies ranging from 500 to 4,000 Hz (Riedner, Levin, & Holliday, 1980; Shapiro, Pikus, Weiss, & Rowe, 1982). Sensorineural hearing loss in general results from an inability in the cochlea or the vestibulocochlear nerve to properly translate soundwaves into electrical impulses and then transmit those impulses to the brainstem. One study suggested that OI-related sensorineural hearing loss results from the atrophy of the hair cells in the cochlea, the atrophy of the stria vascularis, and abnormal bone formation in the cochlea due to increased risk of fracture; however, the exact etiology of sensorineural hearing loss has not been determined conclusively (Swinnen, De Leenheer, Coucke, Cremers, &

Dhooge, 2009). Mixed hearing loss results from a combination of both conductive and sensorineural hearing loss.

To better understand the etiology of sensorineural hearing loss and to develop more successful treatments for patients with OI, an in-depth examination of the temporal bone is required to fully understand how OI-induced changes in the bone structure result in hearing loss. A previous study examined the structure of the temporal bones using CT imaging (Swinnen et al., 2009). However, this study was limited to examining the structures in 2-D, and to the best of my knowledge, no study has examined the 3-D structure of OI temporal bone. The aim of this study was to quantify 3-D structural changes in the cortical bone of the cochlea to better understand how OI causes hearing loss. This was done by examining the intracortical porosity and structure of the cochlea from the *oim* mouse model of OI using synchrotron computed tomography (SR-CT) images at high resolution. The ultimate goal of this study was to gain a more thorough understanding of the relationship between bone morphology and function in order to aid physicians and scientists in developing more effect treatments for patients with OI.

4.2 Cochlea Anatomy

One of the primary components of the inner ear is the cochlea. The cochlea is a spiral shaped bone that resembles a snail shell (Figure 17). The cochlea is located at the end of the inner ear and coils around a central conical rod of spongy bone called the modiolus. Initially, the coil starts at the wide end of the cochlea and gradually shrinks as it winds around the modiolus to reach its apex. The wide end is known as the basal end of the coil, and the apex is referred to as the apical end of the coil. A boney bridge called the osseous spiral lamina projects outward from the modiolus towards the outer wall of the cochlea. The osseous spinal lamina is porous to allow blood vessels and nerves to innervate the cochlea.

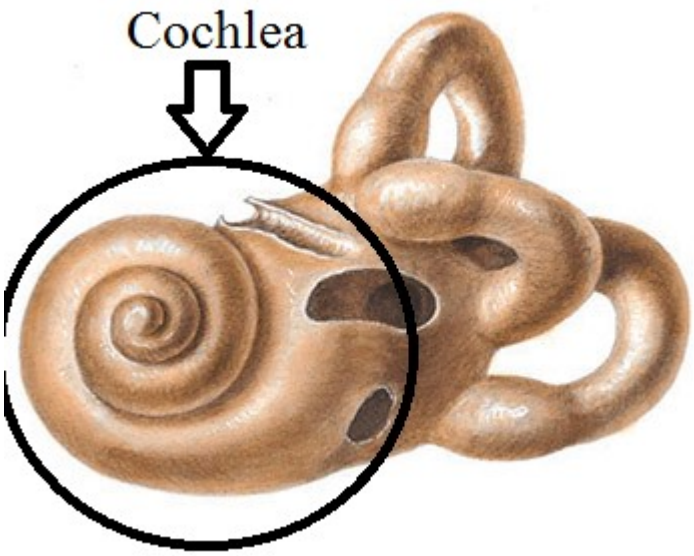

Figure 17. Artistic representation of the inner ear with the cochlea circled in black ("Apologetics Press - The Intricate and Masterful Design of the Human Ear,").

A membrane projecting from the osseous spiral lamina and connecting to the outer wall of the cochlea separates the inner canal in the cochlea into three separate compartments. This membrane houses a middle fluid-filled compartment, known as the scala media. The fluid in the scala media is the endolymph, while the other two fluid-filled canals are the scala vestibule and the scala tympani. The scala media is separated from the scala vestibule by a portion of the membrane called Reissner's membrane, from the outer wall of the cochlea by the stria vascularis, and from the scala tympani by a portion of the membrane called the baslar membrane. The portion of the cochlea which translates sound waves into electrical impulses that are sent to the brain and interpreted as sounds is called the organ of corti. The organ of corti is housed in the scala media and is supported by the basilar membrane. It consists of sensory cells, structural cells, and a firm membrane called the tectorial membrane. The sensory cells, called the inner

and outer hair cells, send electrical impulses to the brain when little hairs, known as the stereo cilia, are disturbed by sound waves. The hairs of the stereo cilia are connected to the tectorial membrane, an arrangement which holds them in a state of tension. This tension enables the stereo cilia to oscillate when disturbed by sound waves. These sensory cells are supported by structural cells known as the outer pillar cells, the inner pillar cells, and the phalangeal cells. These cells line the entire labyrinth of the cochlea and enable the cochlea to detect different frequencies of sound waves. The cochlea is the final component of the hearing system that allows sound waves to be converted into the sensation of hearing. The anatomy that is described here is summarized below in Figure 18.

Because the cochlea plays a crucial role in hearing, the aim of this study was to quantify 3-D structural changes in the cortical bone of the cochlea to better understand how OI might cause hearing loss. This was done by examining the intra cortical porosity and structure of the cochlea from the *oim* mouse model of OI SR-CT was used specifically in this study to obtain high resolution images of the cochlea that could be reconstructed to analyze the morphology of the lacunae with a degree of accuracy that would not be achieved with μCT alone. An increased understanding of the relationship between bone morphology, mechanics, and function can be obtained by increasing the resolution of the cochlea bone images to investigate more accurate models of the bone morphology.

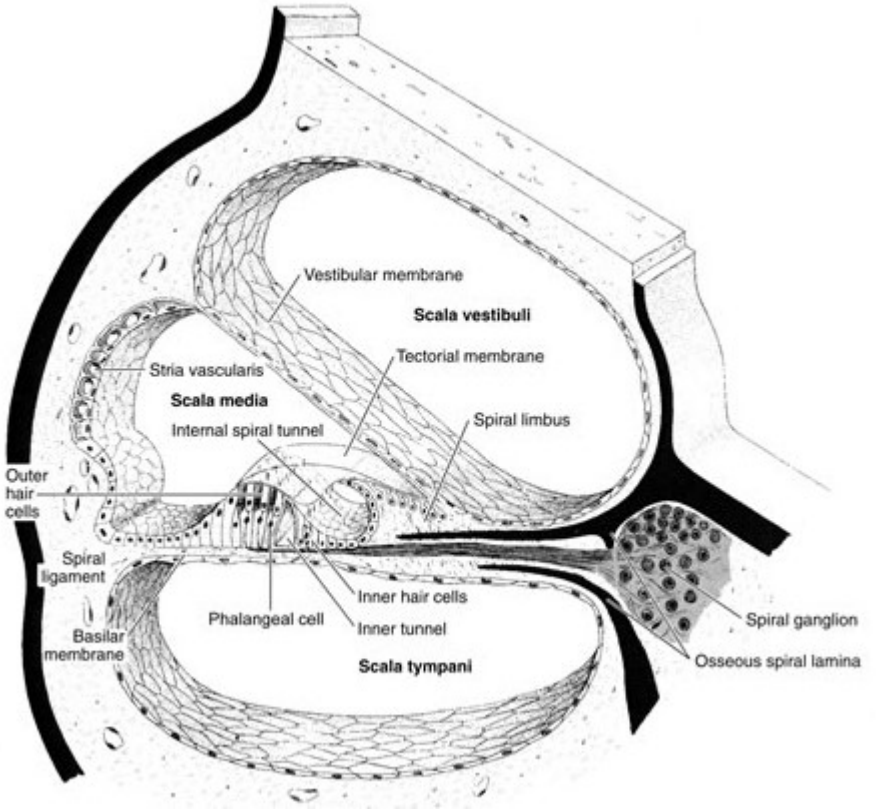

Figure 18. Cross section schematic of the cochlea, depicting the major anatomical components of the cochlea. These components include the three major canals of the cochlea: the scala media, the scala bestibuli, and the scala tympani, the membranes which separate the canals: the bestibular membrane, the stria vascularis, and the basilar membrane, and the organ of corti, which consists of inner and outer hair cells, phalangeal cells, and the tectorial membrane ("neural control and coordination - Online CBSE textbooks,").

4.2 Materials and Methods

4.2.1 Animals

The osteogenesis imperfecta murine *(oim)* mouse model (B6C3Fe a/a-Col1a2$^{oim/oim}$) was selected for this study because the OI symptoms observed in this mutated C57BL/6-C3HeB/Fe mouse hybrid are similar to

those found in the most debilitating non-lethal forms of OI observed in humans (OI type III) (Chipman et al., 1993). These mice exhibit early onset osteopenia because of the mutations in the proα2 chain of type I collagen. These mutations cause the normal strain of proα chains to be altered from two proα1 chains and a proα2 chain to three proα1 chains and cause increased fragility and impaired skeletal growth due to increased cortical thinning and altered porosity (Alessandra Carriero et al., 2014).While it is still unknown if the *oim* mouse model experiences hearing loss, the similarities in the symptoms exhibited by this mouse model and those observed in type III OI suggest that it potentially could experience such a loss, and is therefore a good model for investigating OI-related deafness.

4.2.2 Image Processing

For this study, six WT mice (C57BL/6) and six *oim* mice, all male, were raised to 8 weeks of age before being euthanized per local ethical review and Home Office approval (UK). Following euthanization, the entire inner ear bone was dissected, and the distal end was embedded in bone cement (PMMA) so that the longitudinal axis of the cochlea was aligned vertically. Then the bone was wrapped in gauze that was soaked in phosphate buffered saline (PBS) and stored at -20°C to preserve the structural integrity of the bone and prevent the bone tissue from drying out and degrading. The bones were then taken to the I13-2 beamline Diamond Light Source (UK) to be scanned. Prior to scanning, the bones were allowed to thaw and then placed on the stage of the I13-2 beamline so that the longitudinal axis was parallel to the rotating axis of the stage. The bones were then scanned using SR-CT scans to obtain high-resolution 3-D grayscale images of both the WT and *oim* cochlea. The scans were taken with a nominal resolution of 810 nm using a coupled system consisting of pco.edge 5.5 camera (2,560 x 2,160 pixels, field of view 2.1 x 1.8 mm), a $CdWO_4$ scintillator, and a visual light microscope. For each cochlea, a

filtered polychromatic ‘pink’ beam ranging in energy intensity from 5 to 35 keV with a mean energy of 15 keV was used to obtain 3,001 projections with an exposure time of 30 ms over a 180° range. Tomograms were then reconstructed using filtered back-projection to obtain 3-D image volumes that consisted of 2,159 images for a total voxel volume of 2,560 x 2,160 x 2,159.

The cochlear cortical bone and the intracortical lacuna and canal porosity were segmented for quantitative analysis using the procedure represented in Figure 19. First, the grayscale images were loaded into an open source image analysis software (ImageJ), and a histogram-based global thresholding technique was used to segment the bone matrix from the PBS and soft tissue (Figure 19.A). This technique used an iterative intermeans algorithm to select a threshold based on the mean foreground and background pixel values (Ridler & Calvard, 1978). Thresholding the images resulted in a binary image that displayed the foreground (the cortical bone) in black and the background (the intracortical porosity, soft tissue, and PBS) in white (Figure 19.B). The intracortical porosity that was still connected to the air was segmented manually for each bone using ImageJ. Noise was also manually removed from each image to reduce error in the quantitative analysis of the cochlea intracortical structure (Figure 19.C). The stacks of images were then duplicated and the holes in the duplicate stack of the binary images were filled (Figure 19.D). This stack was used to analyze the cortical bone for each bone. Then a SUBTRACT mathematical operation was used to subtract the cortical bone images from the binary images with the intracortical porosity to obtain images of the lacunae and canals embedded in the cortical bone (Figure 19.E). The Particle Analyzer subroutine from the BoneJ plugin of ImageJ, was then used to segment the intracortical porosity particles by volume, and it created two stacks of images for morphometric analysis: one for the lacunae (100-6600 μm^3) and

one for the canals (> 6600 μm^3) (Figure 19.F and G) (Doube et al., 2010). The stack of images represented in the intracortical canals was further processed by decomposing the canal network into single elements, and they were then analyzed using the skeletonization tools in BoneJ (Skeletonize3D & Analyze Skeleton) (Figure 19.H).

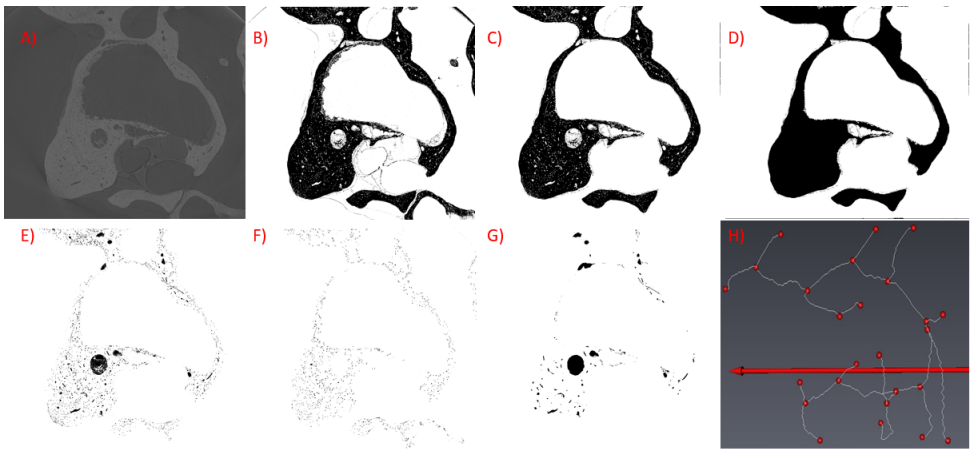

Figure 19. Graphical representation of image segmentation process applied on a representative 2D slice of the 3D stack of images. **A)** Original grayscale image of the bone **B)** Bone after the global thresholding was applied **C)** The manually edited image where the intracortical porosity connected to the PBS was segmented and the noise was removed **D)** Cortical bone (with the intracortical porosity filled in) **E)** Lacunae and intracortical canals after the cortical bone images were subtracted from the images with the intracortical porosity **F)** and **G)** show the separation between canals and lacunae **H)** Skeletonization of a single canal.

The properties of the cortical bone that were evaluated in this study were the cortical thickness (Ct.Th), cortical total volume (Ct.TV), cortical total pore volume (Po.V), and cortical porosity (Ct.Po = Po.V/Ct.TV) at the micro-scale length. Intracortical canal porosity and architecture was

investigated by measuring the number of canals (N.Ca), canal number density (N.Ca/Ct.TV), total canal volume (Ca.V), canal porosity (Ca.V/Ct.TV), canal connectivity density (Ca.ConnD = Ca.Conn/Ct.TV), mean canal volume (<Ca.V>=Ca.V/Ca.N), mean canal diameter (<Ca.D>), and mean canal length (<Ca.Le>) (Schneider et al., 2007). The number of lacunae (N.Lc), lacunar number density (N.Lc/Ct.TV), total lacunar volume (Lc.V), lacunar porosity (Lc.V/Ct.TV), and mean lacuna volume (<Lc.V>=Lc.V/N.Lc) were the morphometric measures used to evaluate the properties of the WT and *oim* lacunae (A. Carriero, M. Doube, et al., 2014). The shape and orientation of the lacunae was also evaluated using measurements obtained by generating a surface mesh around the voxels representing each lacunae using a marching cubes method and then calculating the best-fit ellipsoids around the major [Lc.λ1], intermediate [Lc.λ2], and minor [Lc.λ3] axes using the vertices of the mesh as input in an ellipsoid-fitting algorithm (Doube et al., 2010; Schmid, Schindelin, Cardona, Longair, & Heisenberg, 2010). These measurements were the mean lacunar equancy (sphericity) (<Lc.Eq>=<Lc.λ3/Lc.λ1>), mean lacunar elongation (<Lc.El>=<1- Lc.λ2/Lc.λ1>), and mean lacunar flatness (<Lc.Fl>=<1- Lc.λ3/Lc.λ2>). Finally, the mean lacunar orientation about the longitudinal axis of the bone (<Lc.θ>) was estimated by considering the angle between the lacuna major axis and the longitudinal axis of the cochlea (Carter et al., 2013; Doube et al., 2010).

4.2.3 Statistical Analysis

The measurements obtained from evaluating the morphometric data were analyzed for statistically significant differences using a specialized statistical software package (SPSS, IBM, Somers, NY). Measurements that had the same number of samples between the WT and *oim* groups and that had normal distributions were evaluated using the Student's independent t-

test, while the measurements that had the same number of samples between test groups that did not have normal distributions were evaluated using the Mann-Whitney rank test. The measurements which did not have the same number of samples between groups, such as the mean properties of the lacunae and canals, were evaluated using multilevel linear models; these types of statistical models consider both the number of samples and the dependence between them, and they do not need to assume homogeneity of the data or that the data has a Gaussian distribution. For these measurements, the data was organized into a two level-hierarchy: 'strain' (WT/*oim*) and 'sample' (bone number). A one-sided beta/type II error test was employed for samples which were not found to be statistically significant. This test was used to determine how many samples would be needed to truly determine whether there is an actual difference between groups. For these calculations, the value of α was chosen as 0.05, and the power of the test was set to 0.80.

4.3 Results

The results of the morphometric evaluation show that there was a statistically significant increase in the porosity of the *oim* cortical bone, number of canals, canal porosity, and canal connectivity compared to WT counterparts (Table 7). These results indicate that the *oim* cochlea was more porous with an increased network of larger canals. The remaining morphological differences between the WT and *oim* groups were not statistically significant. However, the power analysis showed that Ct.TV, N.Ca, and N.Lc/Ct.TV could have been evaluated for statistical significance given a reasonably larger sample size. Thus, it is possible that these parameters could also be significantly different between the *oim* and WT cochlea.

Morphometric index	WT N = 6 bones 32,469 canals 884,165 lacunae	*oim* N = 6 bones 54,000 canals N = 918,357 lacunae	*p*-value WT vs. *oim*	Power Test Sample Size
Ct.TV (mm^{-3})	1.03 ± 0.11	0.97 ± 0.10	n.s.	42
Po.V/Ct.TV (%)	5.46 ± 1.53	8.25 ± 0.83	< 0.05	N.A.
N.Ca	5,412 ± 2,757	9,000 ± 4,259	n.s.	18
N.Ca/Ct.TV (mm^{-3})	5,352 ± 2,729	9,015 ± 3,610	<0.05	N.A.
Ca.V/Ct.TV (%)	3.09 ± 0.95	5.75 ± 0.93	<0.05	N.A.
Ca.Conn.D (mm^{-3})	2,736 ± 1,410	4,624 ± 1,873	<0.05	N.A.
<Ca.V> ($10^3 \mu m^3$)	6.67 ± 2.22	7.28 ± 3.09	n.s.	318
<Ca.D> (μm)	12.25 ± 2.88	12.14 ± 3.24	n.s.	10,728
<Ca.Le> (μm)	32.67 ± 38.90	29.94 ± 33.53	n.s.	2,511
N.Lc	147,382 ± 16,826	153,058 ± 23,848	n.s.	219
N.Lc/Ct.TV (mm^{-3})	144,052 ± 20,326	158,360 ± 26,372	n.s.	43
Lc.V/Ct.TV (%)	2.37 ± 0.67	2.50 ± 0.78	n.s.	446
<Lc.V> (μm^3)	163.39 ± 103.20	156.89 ± 104.76	n.s.	3,212
<Lc.Eq> (1)	0.363 ± 0.138	0.378 ± 0.135	n.s.	1,047
<Lc.El> (1)	0.197 ± 0.100	0.200 ± 0.099	n.s.	13,740
<Lc.Fl> (1)	0.529 ± 0.206	0.510 ± 0.201	n.s.	1,454
<Lc.θ> (deg)	78.83 ± 37.97	79.68 ± 42.87	n.s.	31,454

Table 10. Data from the morphological analysis of the lacunae, canals, and cortical bone volumes were obtained from the reconstructed SR-CT images. From these results, it was observed that the *oim* cortical bone was more porous and that the canals were more numerous and interconnected. Results from the one-sided beta/type-II error test are listed for the non-significant parameters to determine what sample size would be required to properly evaluate statistical significance.

4.4 Discussion

This study quantitatively assessed the 3-D morphometrical porosity of osteogenesis imperfecta *oim* cochlea bone using SR-CT. Our results demonstrated that the *oim* cochlea had increased porosity with increased canal porosity, size, and architecture. This increased porosity and canal architecture may be due to altered metabolic functioning in the *oim* mice which increases the rate of bone turnover (Zhang, Doty, Hughes, Dempster, & Camacho, 2007). Increased vascular porosity has been previously related to reduced fracture toughness in bone (Yeni et al., 1997). More recent studies on long bones have also shown that intracortical bone architecture can influence fracture initiation and propagation(Alessandra Carriero et al., 2014; A. Carriero, E. A. Zimmermann, et al., 2014). Increased porosity increases the areas of local stress and strain concentrations within the bone, which in turn increases crack propagation within the bone, dramatically decreasing its toughness (Alessandra Carriero et al., 2014; A. Carriero, E. A. Zimmermann, et al., 2014; Yeni et al., 1997). This makes the bone more susceptible to fractures. Thus, the changes in the cochlea intracortical architecture may cause hearing loss by affecting bone mechanical integrity and increasing the risk of fracture and deformities in the bone. This is because fractures and bone deformations would adversely affect the sound conductivity in the cochlea by preventing sound waves from being properly transmitted through the organ of corti to the temporal lobe of the brain.

The observations that the *oim* cochlea have larger, more interconnected canals, and greater overall porosity agree with a prior study which investigated the canal networks in human OI cortical bone (Jameson, Albert, Busse, Smith, & Harris). In that study, the 3-D structure of pediatric cortical bone fragments were analyzed using images generated using microtomography with a synchrotron light source (SRμCT). The results

from this study suggested that the increased pore network in OI was the primary contributor to the observed reductions in mechanical properties.

Furthermore, the results of the one-sided beta/type-II error test suggested that the cortical bone volume, number of canals, and lacunae density may also be significantly altered, given a larger sample size. Thus, while these parameters did not come to be significantly altered in our study, there is a trend that suggests that the cortical bone volume is decreased and that the number of canals and lacunae density are increased in the *oim* cochlear bone. However, because this study was the first to analyze the cochlea in such detail, the sample size was limited to a preliminary set of 6 samples per group for analysis.

The results obtained in this study correlate positively with the results obtained from another previous study which was performed on long bones of *oim* mice (A. Carriero, M. Doube, et al., 2014). The morphometric analysis of the cortical bone, canal network, and osteocyte lacunae of *oim* long bones demonstrated a few similarities between the *oim* long bones and cochlea: both types of bone exhibited more branched canals, while the results from the one-sided beta/type-II error test suggest that number of canals and the lacunae density would be greater in both types of bone, given a larger sample size. However, there were also some differences between the long bones and the cochlea: the total cortical porosity was similar between the *oim* and WT lone bone, while in this study, the cortical porosity was significantly increased in the *oim* cochlea. Additionally, in the *oim* long bone, there were observed differences in the lacunae shape and orientation, while here there were no statistically significant differences between the WT and *oim* bone. However, the finding that there are differences between the morphology of the cortical bone, intracortical canals, and lacunae in the long bones and the cochlea is not necessarily surprising. Previous studies have shown that the mechanisms which control bone remodeling in the

cochlea are different from the remodeling mechanisms in the long bones, with the bone in the cochlea being remodeled at a much slower rate compared to other bones in the body (Jáuregui et al., 2016). One possible explanation for the increased cortical porosity is that the altered collagen in the bone due to OI degrades much faster than normal and signals increased osteoclast resorption in the cochlea. Furthermore, due to its anatomical location within the body, the cochlea experiences lower amplitudes of mechanical loading compared to long bone (Vatsa et al., 2008). In the long bone, the mechanical forces which act on the lacunae stimulate them to change shape and orient themselves in the direction of mechanical loading. However, because the lacunae in the cochlea do not experience this mechanical stimulation, there is no change in shape or orientation.

4.5 Conclusions

The SR-CT imaging analysis of the cochlea in this study revealed that the cochlear *oim* bone has increased vascular porosity with larger and more branched canals, resulting in a greater overall intracortical porosity. Since bone fractured toughness is reduced in the presence of increased vascular porosity, it is reasonable to conclude that there are increased risks of bone fractures in the *oim* cochlea. This, in turn, could potentially cause deformations to the cochlea structure, changing the shape of the canals which conduct soundwaves to the organ of corti. These deformations could result in hearing loss by preventing sound from being transmitted properly. The deformations caused by these fractures could also cause damage to the organ of corti itself, further increasing the risk of hearing loss. While further investigation is needed to verify this hypothesis, the results presented here help provide a more thorough insight into understanding how OI causes hearing loss and could lead to improved methods of patient treatment.

Chapter 5

Overview and Scientific Contributions

5.1 Outcomes and Contributions to the Understanding of Bone

In this thesis, two studies were performed in which the mechanical, structural, and compositional properties of bone from genetically altered mice were investigated to obtain better understanding of how genetic alterations affect the mechanical integrity of bone.

In the first study, which was discussed in chapter 3, the effect of TIMP-3 deficiency on bone properties was examined using a mouse with TIMP-3 encoding gene suppression. A series of characterization techniques were employed to evaluate bone quality in terms of mechanical, structural, and compositional metrics in a multiscale fashion. The yield and ultimate load, stiffness, work to yield, and yield and ultimate stress values in the *Timp-3*$^{-/-}$ mice were significantly reduced. These results correlated with altered geometric properties such as decreased bone volume, cross sectional area, cortical thickness, moments of inertia, tissue mineral density, and bone mass, as well as increased cortical porosity. Furthermore, the reduced mechanical properties also correlated with decreases in carbonate content, acid phosphate content, and the heterogeneity of the collagen crosslinking in the cortical bone as well as a reduced carbonate content, a reduction in mature to immature collagen cross link ratio, and changes in the heterogeneity of the carbonate, collagen cross link ratio, and crystallinity. These results show that TIMP-3 deficiency compromises the mechanical integrity by altering bone geometry and composition at the tissue level. Because TIMP-3 inhibits MMP activity, it is believed that TIMP-3 deficiency results in excessive MMP activity, which may in turn accelerate

bone remodeling. An increase in bone remodeling may explain the changes in structure and composition observed in TIMP-3 deficient bones, and their inferior mechanical properties. This research demonstrates the importance of sustaining proper levels of TIMP-3 in the bone to maintain mechanical integrity.

In the second study, presented in chapter 4, there was an examination of the cochlear bone microstructure in a mouse model of osteogenesis imperfecta using SR-CT scans acquired at the Diamond Light Source. The analysis of the images revealed that intracortical porosity is higher in OI cochlea due to an increase in size and connectivity of the intracortical vascular canals. Because bone with high porosity has low toughness, and fractures generate bone deformities in OI due to poor bone healing, the results of this study suggest that hearing loss often occurs in patients with osteogenesis imperfecta because of the increased likelihood of fractures in their cochlea that affect the cochlea's ability to conduct sound waves to the organ of corti. This information can help clinicians and researchers better understand how to prevent hearing loss in patients with osteogenesis imperfecta. Overall, both studies demonstrate the important role of genes in developing and maintaining bone integrity. Bone itself is a strong and tough material that articulates at different length scales. However, changes in the structure and composition of the bone, even at the nano- scale, can ramify to higher levels of the hierarchy and can significantly compromise the mechanical integrity of the bone and its function. Therefore, due to the bone's hieratical structure, skeletal pathologies must be treated from the smallest scale length up to maintain or improve bone health.

5.2 Future Work

The studies presented in this thesis demonstrated that genetic alterations result in changes in the mechanical, geometric, and

compositional bone properties. However, for both studies that were conducted, further investigation is required in order build a more comprehensive understanding of how these genetic alterations effect bone structure.

For the first study, the mechanical and material properties of the long and short bones of *Timp-3*$^{-/-}$ and WT mice were examined at the macro-scale level using 3-point bending, notched 3-point bending, and compression testing, while the geometric properties at the micro-scale level were evaluated using μCT image analysis. FTIR-I was used to access the compositional properties of the bone at the nano-scale level. These techniques demonstrated that the genetically altered *Timp-3*$^{-/-}$ mice had reduced mechanical properties and altered geometry and composition and suggested that these observations may be a result of altered bone remodeling due to increased MMP activity; however, this study did not examine markers for osteoblast and osteoclast activity or for MMP levels to determine how these biological factors might play a role in linking TIMP-3 deficiency to the changes in bone properties. Thus, future studies will be needed to be able to quantify these biological factors. Osteoclast activity can be evaluated using tartrate resistant acid phosphatase (TRAP) staining to analyze bone histology at the micro-scale level (Javaheri et al., 2016). An alkaline phosphatase (ALP) assay can be used to measure osteoblast activity by measuring the alkaline phosphatase osteoblast biomarker in bone tissue culture samples (Sabokbar, Millett, Myer, & Rushton, 1994). The MMP activity could also be evaluated using a commercially available red fluorometric MMP activity assay kit. This kit could be used to evaluate the activity of MMPs-1, -2, -8, -9, -13, and -14, given their perceived role in collagen degradation and bone tissue remodeling.

The properties of the of the *Timp-3*$^{-/-}$ bone need to be further quantified at each scale length. The study presented in this thesis

investigated the mechanical properties of the bone at the macro-scale length, but a comprehensive understanding of the bone mechanics requires knowledge at the micro- and nano-scale levels as well. Micro-indentation could be used to evaluate the bone mechanics at micro-scale and nano-indentation could be used to evaluate the bone mechanics at the nano-scale. A micro-indentation tip could be affixed to the linear actuator of a Bose ElectroForce mechanical test instrument while nano-indentation could be performed using an atomic-force microscope.

The geometric properties of the bone at the nano-scale level could also be investigated with more precision than with μCT using x-ray scattering techniques such as small-angle x-ray scattering (SAXS) or wide-angle x-ray diffraction (WAXD) to evaluate the crystalline structure of the hydroxyapatite mineral. This would provide valuable insight into how mineralization occurs in TIMP-3 deficient bone, and how the size, shape, and orientation of the mineral effects bone mechanical properties.

The composition of the *Timp-3*$^{-/-}$ bone could also be examined at the micro-scale level using a specific technique called backscattered electron microscopy (BSE SEM) to evaluate the degree of mineralization. Thermogravimetric analysis (TGA) could be used to determine the bulk mineral-to-matrix ratio of the bone at the macro-scale level [Rodriguez-Florez, et al., 2015]. Finally, polarized light microscopy could be employed to investigate the fiber orientation of the collagen in TIMP-3 deficient bone to determine whether changes in the fiber alignment might help explain the decreased mechanical and material properties observed in this study (Bakbak et al., 2011).

For the second study, the mechanics of the cochlea could be further assessed by analyzing the distribution of stresses and strains present in the cochlear cortical bone when a hydrostatic pressure is applied to the surfaces

of the semicircular canals in the cochlea. This could be accomplished by constructing a CAD model of the cortical bone from the reconstructed nano-CT scans and then importing that CAD model into a finite element modeling (FEM) software, applying the appropriate boundary conditions, and performing the analysis to evaluate stress and strain. The CAD model is constructed by a multi-step process involving several open source and commercially available software packages (Kumara, 2011). The first step in analyzing the stress and strain distributions in the cochlea would be to compile the images into a stack using open source software (ImageJ) and then importing that stack as a .stl file into a mesh editing software (MeshLab) to be refined and smoothed through a series of filters. Once the stl mesh was refined, it could then be imported into a commercially available CAD modelling software (Rhino 5.0) that could convert the mesh into a .sat file that could be read by commercially available FEM software packages like ANSYS. Once the CAD model had been generated, it could be imported into ANSYS and assigned material properties based on prior research which attempted to model the human cochlea using FEM (L. Xu, Huang, Ta, Rao, & Tian, 2015). Once the material properties had been assigned, the model would be meshed and loading conditions would be applied. The cochlea would be assigned a fixed boundary condition at the basal end of the coil and a hydrostatic pressure would be applied to the interior of the canals in the cochlea. The analysis could then be conducted to determine whether the structure of the *oim* cochlea would alter the distribution and magnitude of the induced stresses and strains. Finally, in addition to modelling the mechanics of the cochlea using FEM, BSE SEM analysis could also be performed on the SR-CT scans to evaluate the mineralization of the *oim* bone. This would then be correlated to the changes in the mechanics of the cochlear bone observed by performing the FEM analysis.

In both studies, the bone disorders were the result of alterations or mutations of normal genes, indicating the important role that genes play in ultimately determining bone health. Interestingly, in both cases, the genetic abnormalities seemed to primarily influence bone health by altering bone remodeling. This suggests that there is a very precise range in which the rate of bone remodeling can be considered “healthy”, and if the rate falls outside of that range, it is detrimental to the overall health of the bone. If there is an imbalance in the rates of bone formation and resorption, then too much or too little bone can form which alters the bone properties. These changes then affect the overall bone strength. Therefore, to develop treatments for diseases related to TIMP-3 deficiency or OI, biomedical engineers, scientists, and physicians need to begin developing medical treatments for skeletal diseases by addressing the problems in bone health at a genetic level.

References

Alberts, B., Johnson, A., Lewis, J., Raff, M., Roberts, K., & Walter, P. (1997). Molecular Biology of the Cell (Garland Science, New York, 2002). *There is no corresponding record for this reference*.

[Apologetics Press - The Intricate and Masterful Design of the Human Ear]). Web Page.

Augat, P., & Schorlemmer, S. (2006). The role of cortical bone and its microstructure in bone strength. *Age and Ageing, 35 Suppl 2*, ii27-ii31. doi:35/suppl_2/ii27 [pii]

Babatunde, O. M., Fragomen, A. T., & Rozbruch, S. R. (2010). Noninvasive quantitative assessment of bone healing after distraction osteogenesis. *HSS journal, 6*(1), 71-78.

Bakbak, S., Kayacan, R., & Akkuş, O. (2011). Effect of collagen fiber orientation on mechanical properties of cortical bone. *Journal of Biomechanics, 44*, 11.

Baker, A. T., Ramshaw, J. A., Chan, D., Cole, W. G., & Bateman, J. F. (1989). Changes in collagen stability and folding in lethal perinatal osteogenesis imperfecta. The effect of alpha 1 (I)-chain glycine-to-arginine substitutions. *The Biochemical journal, 261*(1), 253-257.

Barbier, A., Martel, C., De Vernejoul, M. C., Tirode, F., Nys, M., Mocaer, G., . . . Lacheretz, F. (1999). The visualization and evaluation of bone architecture in the rat using three-dimensional X-ray microcomputed tomography. *Journal of bone and mineral metabolism, 17*(1), 37-44.

Barkaoui, A., Chamekh, A., Merzouki, T., Hambli, R., & Mkaddem, A. (2014). Multiscale approach including microfibril scale to assess elastic constants of cortical bone based on neural network computation and homogenization method. *Int J Numer Method Biomed Eng, 30*(3), 318-338. doi:10.1002/cnm.2604

Bell, K. L., Loveridge, N., Power, J., Rushton, N., & Reeve, J. (1999). Intracapsular hip fracture: increased cortical remodeling in the thinned and porous anterior region of the femoral neck. *Osteoporosis International, 10*(3), 248-257.

[Bone Structure and Function]). Web Page.

[bonestructure.gif (GIF Image, 823 × 703 pixels)]). Web Page.

Bonnans, C., Chou, J., & Werb, Z. (2014). Remodelling the extracellular matrix in development and disease. *Nature reviews Molecular cell biology, 15*(12), 786-801.

Bonnet, N., Laroche, N., Vico, L., Dolleans, E., Courteix, D., & Benhamou, C. L. (2009). Assessment of trabecular bone microarchitecture by two different x-ray microcomputed tomographs: a comparative study of the rat distal tibia using Skyscan and Scanco devices. *Medical physics, 36*(4), 1286-1297.

Botter, S. M., Glasson, S. S., Hopkins, B., Clockaerts, S., Weinans, H., van Leeuwen, J., & van Osch, G. (2009). ADAMTS5−/− mice have less subchondral bone changes after induction of osteoarthritis through surgical instability: implications for a link between cartilage and subchondral bone changes. *Osteoarthritis and Cartilage, 17*(5), 636-645.

Bouxsein, M. L. (2005). Determinants of skeletal fragility. *Best practice & research Clinical rheumatology, 19*(6), 897-911.

Bouxsein, M. L., Boyd, S. K., Christiansen, B. A., Guldberg, R. E., Jepsen, K. J., & Müller, R. (2010). Guidelines for assessment of bone microstructure in rodents using micro–computed tomography. *Journal of bone and mineral research, 25*(7), 1468-1486.

Brew, K., Dinakarpandian, D., & Nagase, H. (2000). Tissue inhibitors of metalloproteinases: evolution, structure and function. *Biochimica et Biophysica Acta (BBA)-Protein Structure and Molecular Enzymology, 1477*(1), 267-283.

Brew, K., & Nagase, H. (2010). The tissue inhibitors of metalloproteinases (TIMPs): an ancient family with structural and functional diversity. *Biochimica et Biophysica Acta (BBA)-Molecular Cell Research, 1803*(1), 55-71.

Bruni-Cardoso, A., Johnson, L. C., Vessella, R. L., Peterson, T. E., & Lynch, C. C. (2010). Osteoclast-derived matrix metalloproteinase-9 directly affects angiogenesis in the prostate tumor-bone microenvironment. *Molecular cancer research : MCR, 8*(4), 459-470. doi:10.1158/1541-7786.MCR-09-0445 [doi]

Byers, P. H., & Cole, W. G. (2002). Osteogenesis imperfecta. *Connective tissue and its heritable disorders: molecular, genetic and medical aspects*, 385-430.

Carriero, A., Doube, M., Vogt, M., Busse, B., Zustin, J., Levchuk, A., . . . Shefelbine, S. J. (2014). Altered lacunar and vascular porosity in osteogenesis imperfecta mouse bone as revealed by synchrotron tomography contributes to bone fragility. *Bone, 61*, 116-124.

Carriero, A., Zimmermann, E. A., Paluszny, A., Tang, S. Y., Bale, H., Busse, B., . . . Shefelbine, S. J. (2014). How tough is brittle bone? Investigating osteogenesis imperfecta in mouse bone. *Journal of Bone and Mineral Research, 29*(6), 1392-1401.

Carriero, A., Zimmermann, E. A., Shefelbine, S. J., & Ritchie, R. O. (2014). A methodology for the investigation of toughness and crack propagation in mouse bone. *J Mech Behav Biomed Mater, 39*, 38-47. doi:10.1016/j.jmbbm.2014.06.017

Carter, Y., Thomas, C. D. L., Clement, J. G., Peele, A. G., Hannah, K., & Cooper, D. M. L. (2013). Variation in osteocyte lacunar morphology and density in the human femur—a synchrotron radiation micro-CT study. *Bone, 52*(1), 126-132.

Chappard, D., Retailleau-Gaborit, N., Legrand, E., Baslé, M. F., & Audran, M. (2005). Comparison insight bone measurements by histomorphometry and μCT. *Journal of Bone and Mineral Research, 20*(7), 1177-1184.

[Chapter 6: Bones and Skeletal Tissues]). Web Page.

[Characterizing the mechanical properties of bone with the assistance of digital light microscopy]). Web Page.

Chipman, S. D., Sweet, H. O., McBride, D. J., Jr., Davisson, M. T., Marks, S. C., Jr., Shuldiner, A. R., . . . Shapiro, J. R. (1993). Defective pro alpha 2(I) collagen synthesis in a recessive mutation in mice: a model of human osteogenesis imperfecta. *Proceedings of the National Academy of Sciences of the United States of America, 90*(5), 1701-1705.

Cole, W. G. (1998). The Molecular Pathology of Osteogenesis Imperfecta. *Advances in Orthopaedic Surgery, 21*(5), 321-321.

Cole, W. G. (2002). Advances in osteogenesis imperfecta. *Clinical orthopaedics and related research, 401*, 6-16.

[Collagene]). Web Page.

Compston, J. (2006). Bone quality: what is it and how is it measured? *Arq Bras Endocrinol Metabol, 50*(4), 579-585.

Cox, T. R., & Erler, J. T. (2011). Remodeling and homeostasis of the extracellular matrix: implications for fibrotic diseases and cancer. *Disease models & mechanisms, 4*(2), 165-178. doi:10.1242/dmm.004077 [doi]

Cruz-Munoz, W., Kim, I., & Khokha, R. (2006). TIMP-3 deficiency in the host, but not in the tumor, enhances tumor growth and angiogenesis. *Oncogene, 25*(4), 650-655.

Cruz-Munoz, W., Sanchez, O. H., Di Grappa, M., English, J. L., Hill, R. P., & Khokha, R. (2006). Enhanced metastatic dissemination to multiple organs by melanoma and lymphoma cells in timp-3−/− mice. *Oncogene, 25*(49), 6489-6496.

Currey, J. D. (1969). The relationship between the stiffness and the mineral content of bone. *Journal of Biomechanics, 2*(4), 477-480.

Delmas, P. D., Tracy, R. P., Riggs, B. L., & Mann, K. G. (1984). Identification of the noncollagenous proteins of bovine bone by two-dimensional gel electrophoresis. *Calcified tissue international, 36*(1), 308-316.

Donnelly, E. (2011). Methods for assessing bone quality: a review. *Clinical Orthopaedics and Related Research®, 469*(8), 2128-2138.

Donnelly, E., Meredith, D. S., Nguyen, J. T., Gladnick, B. P., Rebolledo, B. J., Shaffer, A. D., . . . Boskey, A. L. (2012). Reduced cortical bone compositional heterogeneity with bisphosphonate treatment in postmenopausal women with intertrochanteric and subtrochanteric fractures. *Journal of Bone and Mineral Research, 27*(3), 672-678.

Doube, M., Kłosowski, M. M., Arganda-Carreras, I., Cordelières, F. P., Dougherty, R. P., Jackson, J. S., . . . Shefelbine, S. J. (2010). BoneJ: free and extensible bone image analysis in ImageJ. *Bone, 47*(6), 1076-1079.

Ethier, C. R., & Simmons, C. A. (2007). *Introductory biomechanics: from cells to organisms*: Cambridge University Press.

[Extracellular matrix]). Web Page.

Fanuscu, M. I., & Chang, T. L. (2004). Three-dimensional morphometric analysis of human cadaver bone: microstructural data from maxilla and mandible. *Clinical oral implants research, 15*(2), 213-218.

Federici, M., Hribal, M. L., Menghini, R., Kanno, H., Marchetti, V., Porzio, O., . . . Lauro, R. (2005). Timp3 deficiency in insulin receptor-haploinsufficient mice promotes diabetes and vascular inflammation via increased TNF-alpha. *The Journal of clinical investigation, 115*(12), 3494-3505. doi:10.1172/JCI26052 [doi]

Gajko-Galicka, A. (2002). Mutations in type I collagen genes resulting in osteogenesis imperfecta in humans. *ACTA BIOCHIMICA POLONICA-ENGLISH EDITION-, 49*(2), 433-442.

[Gallery For > Intramembranous Ossification Diagram]). Web Page.

Garnero, P., Ferreras, M., Karsdal, M. A., Nicamhlaoibh, R., Risteli, J., Borel, O., . . . Delaisse, J. M. (2003). The type I collagen fragments ICTP and CTX reveal distinct enzymatic pathways of bone collagen degradation. *Journal of bone and Mineral Research, 18*(5), 859-867.

Giannelli, G., Falk-Marzillier, J., Schiraldi, O., Stetler-Stevenson, W. G., & Quaranta, V. (1997). Induction of cell migration by matrix metalloprotease-2 cleavage of laminin-5. *Science (New York, N.Y.), 277*(5323), 225-228.

Gill, S. E., Pape, M. C., Khokha, R., Watson, A. J., & Leco, K. J. (2003). A null mutation for TissueInhibitor ofMetalloproteinases-3 (Timp-3) impairs murine bronchiole branching morphogenesis. *Developmental biology, 261*(2), 313-323.

Gourion-Arsiquaud, S., Lukashova, L., Power, J., Loveridge, N., Reeve, J., & Boskey, A. L. (2013). Fourier transform infrared imaging of femoral neck bone: Reduced heterogeneity of mineral-to-matrix and carbonate-to-phosphate and more variable crystallinity in treatment-naive fracture cases compared with fracture-free controls. *Journal of Bone and Mineral Research, 28*(1), 150-161.

Haba, Y., Lindner, T., Fritsche, A., Schiebenhofer, A. K., Souffrant, R., Kluess, D., . . . Bader, R. (2012). Relationship between mechanical properties and bone mineral density of human femoral bone retrieved from patients with osteoarthritis. *The open orthopaedics journal, 6*, 458-463. doi:10.2174/1874325001206010458 [doi]

Hammoud, L., Lu, X., Lei, M., & Feng, Q. (2011). Deficiency in TIMP-3 increases cardiac rupture and mortality post-myocardial infarction via EGFR signaling: beneficial effects of cetuximab. *Basic research in cardiology, 106*(3), 459-471.

Hamze, A. B., Wei, S., Bahudhanapati, H., Kota, S., Acharya, K. R., & Brew, K. (2007). Constraining specificity in the N-domain of tissue inhibitor of metalloproteinases-1; gelatinase-selective inhibitors. *Protein Science, 16*(9), 1905-1913.

Hijova, E. (2005). Matrix metalloproteinases: their biological functions and clinical implications. *Bratisl Lek Listy, 106*(3), 127-132.

Hodge, A. J., & Petruska, J. A. (1963). Recent studies with the electron microscope on ordered aggregates of the tropocollagen molecule. *Aspects of protein structure*, 289-300.

Holmbeck, K., Bianco, P., Caterina, J., Yamada, S., Kromer, M., Kuznetsov, S. A., . . . Pidoux, I. (1999). MT1-MMP-deficient mice develop dwarfism, osteopenia, arthritis, and connective tissue disease due to inadequate collagen turnover. *Cell, 99*(1), 81-92.

Huber, M. A. (2007). Osteogenesis imperfecta. *Oral Surgery, Oral Medicine, Oral Pathology, Oral Radiology, and Endodontology, 103*(3), 314-320.

Imani, P., Vijayasekaran, S., & Lannigan, F. (2003). Is it necessary to screen for hearing loss in the paediatric population with osteogenesis imperfecta? *Clinical Otolaryngology & Allied Sciences, 28*(3), 199-202.

Inada, M., Wang, Y., Byrne, M. H., Rahman, M. U., Miyaura, C., Lopez-Otin, C., & Krane, S. M. (2004). Critical roles for collagenase-3 (Mmp13) in development of growth plate cartilage and in endochondral ossification. *Proceedings of the National Academy of Sciences of the United States of America, 101*(49), 17192-17197. doi:0407788101 [pii]

[Introduction of Human Physiology Part2]). Web Page.

Iolascon, G., Napolano, R., Gioia, M., Moretti, A., Riccio, I., & Gimigliano, F. (2013). The contribution of cortical and trabecular tissues to bone strength: insights from denosumab studies. *Clinical cases in mineral and bone metabolism, 10*(1), 47-51.

Jameson, J. R., Albert, C. I., Busse, B., Smith, P. A., & Harris, G. F. (2013). *3D micron-scale imaging of the cortical bone canal network in human osteogenesis imperfecta (OI).* Paper presented at the SPIE Medical Imaging.

Janssen, A., Hoellenriegel, J., Fogarasi, M., Schrewe, H., Seeliger, M., Tamm, E., . . . Stöhr, H. (2008). Abnormal vessel formation in the choroid of mice lacking tissue inhibitor of metalloprotease-3. *Investigative ophthalmology & visual science, 49*(7), 2812-2822.

Javaheri, B., Hopkinson, M., Poulet, B., Pollard, A. S., Shefelbine, S. J., Chang, Y.-M., . . . Pitsillides, A. A. (2016). Deficiency and Also Transgenic Overexpression of Timp-3 Both Lead to Compromised Bone Mass and Architecture In Vivo. *PloS one, 11*(8), e0159657.

Jilka, R. L. (2013). The relevance of mouse models for investigating age-related bone loss in humans. *The journals of gerontology.Series A, Biological sciences and medical sciences, 68*(10), 1209-1217. doi:10.1093/gerona/glt046 [doi]

Jáuregui, E. J., Akil, O., Acevedo, C., Hall-Glenn, F., Tsai, B. S., Bale, H. A., . . . Lustig, L. R. (2016). Parallel mechanisms suppress cochlear bone remodeling to protect hearing. *Bone, 89*, 7-15.

Kapadia, R. D., Stroup, G. B., Badger, A. M., Koller, B., Levin, J. M., Coatney, R. W., . . . Gowen, M. (1998). Applications of micro-CT and MR microscopy to study pre-clinical models of osteoporosis and osteoarthritis. *Technology and Health Care, 6*(5, 6), 361-372.

Kassiri, Z., Defamie, V., Hariri, M., Oudit, G. Y., Anthwal, S., Dawood, F., . . . Khokha, R. (2009). Simultaneous transforming growth factor beta-tumor necrosis factor activation and cross-talk cause aberrant remodeling response and myocardial fibrosis in Timp3-deficient heart. *The Journal of biological chemistry, 284*(43), 29893-29904. doi:10.1074/jbc.M109.028449 [doi]

Kassiri, Z., Oudit, G. Y., Sanchez, O., Dawood, F., Mohammed, F. F., Nuttall, R. K., . . . Khokha, R. (2005). Combination of tumor necrosis factor-alpha ablation and matrix metalloproteinase inhibition prevents heart failure after pressure overload in tissue inhibitor of metalloproteinase-3 knock-out mice. *Circulation research, 97*(4), 380-390. doi:01.RES.0000178789.16929.cf [pii]

Keaveny, T. M., & Hayes, W. C. (1993). Mechanical properties of cortical and trabecular bone. *Bone, 7*, 285-344.

Knott, L., & Bailey, A. J. (1998). Collagen cross-links in mineralizing tissues: a review of their chemistry, function, and clinical relevance. *Bone, 22*(3), 181-187.

Knott, L., Whitehead, C. C., Fleming, R. H., & Bailey, A. J. (1995). Biochemical changes in the collagenous matrix of osteoporotic avian bone. *The Biochemical journal, 310 (Pt 3)*(Pt 3), 1045-1051.

Kuhn, J. L., Goldstein, S. A., Feldkamp, L. A., Goulet, R. W., & Jesion, G. (1990). Evaluation of a microcomputed tomography system to study trabecular bone structure. *Journal of Orthopaedic Research, 8*(6), 833-842.

Kumara, K. P. (2011). Reconstructing Solid Model from 2D Scanned Images of Biological Organs for Finite Element Simulation.

Kuurila, K., Johansson, R., Kaitila, I., & GrêNman, R. (2002). Hearing loss in Finnish adults with osteogenesis imperfecta: a nationwide survey. *Annals of Otology, Rhinology & Laryngology, 111*(10), 939-946.

Leco, K. J., Waterhouse, P., Sanchez, O. H., Gowing, K. L., Poole, A. R., Wakeham, A., . . . Khokha, R. (2001). Spontaneous air space enlargement in the lungs of mice lacking tissue inhibitor of metalloproteinases-3 (TIMP-3). *The Journal of clinical investigation, 108*(6), 817-829. doi:10.1172/JCI12067 [doi]

Li, L., & Li, H. (2013). Role of microRNA-mediated MMP regulation in the treatment and diagnosis of malignant tumors. *Cancer biology & therapy, 14*(9), 796-805.

Lowenstam, H. A., & Weiner, S. (1989). *On biomineralization*: Oxford University Press on Demand.

Lu, P., Takai, K., Weaver, V. M., & Werb, Z. (2011). Extracellular matrix degradation and remodeling in development and disease. *Cold Spring Harbor perspectives in biology, 3*(12), 10.1101/cshperspect.a005058. doi:10.1101/cshperspect.a005058 [doi]

Lukashev, M. E., & Werb, Z. (1998). ECM signalling: orchestrating cell behaviour and misbehaviour. *Trends in cell biology, 8*(11), 437-441.

Manes, S., Llorente, M., Lacalle, R. A., Gomez-Mouton, C., Kremer, L., Mira, E., & Martinez-A, C. (1999). The matrix metalloproteinase-9 regulates the insulin-like growth factor-triggered autocrine response in DU-145 carcinoma cells. *The Journal of biological chemistry, 274*(11), 6935-6945.

Martin, E. L., McCaig, L. A., Moyer, B. Z., Pape, M. C., Leco, K. J., Lewis, J. F., & Veldhuizen, R. A. (2005). Differential response of TIMP-3 null mice to the lung insults of sepsis, mechanical ventilation, and hyperoxia. *American journal of physiology.Lung cellular and molecular physiology, 289*(2), L244-251. doi:00070.2005 [pii]

Martin, E. L., Truscott, E. A., Bailey, T. C., Leco, K. J., McCaig, L. A., Lewis, J. F., & Veldhuizen, R. A. W. (2007). Lung mechanics in the TIMP3 null mouse and its response to mechanical ventilation. *Experimental lung research, 33*(2), 99-113.

Marzia, M., Guaiquil, V., Horne, W. C., Blobel, C. P., Baron, R., & Chiusaroli, R. (2011). Lack of ADAM15 in mice is associated with increased osteoblast function and bone mass. *Biological chemistry, 392*(10), 877-885.

McCalden, R. W., McGeough, J. A., Barker, M. B., & Court-Brown, C. M. (1993). Age-related changes in the tensile properties of cortical bone. The relative importance of changes in porosity, mineralization, and microstructure. *The Journal of bone and joint surgery.American volume, 75*(8), 1193-1205.

McCawley, L. J., & Matrisian, L. M. (2001). Matrix metalloproteinases: they're not just for matrix anymore! *Current opinion in cell biology, 13*(5), 534-540.

McQuibban, G. A., Butler, G. S., Gong, J. H., Bendall, L., Power, C., Clark-Lewis, I., & Overall, C. M. (2001). Matrix metalloproteinase activity inactivates the CXC chemokine stromal cell-derived factor-1. *The Journal of biological chemistry, 276*(47), 43503-43508. doi:10.1074/jbc.M107736200 [doi]

Miller, A. (1984). Collagen: the organic matrix of bone. *Philosophical transactions of the Royal Society of London.Series B, Biological sciences, 304*(1121), 455-477.

Millington-Ward, S., McMahon, H. P., & Farrar, G. J. (2005). Emerging therapeutic approaches for osteogenesis imperfecta. *Trends in molecular medicine, 11*(6), 299-305.

Mohammed, F. F., Smookler, D. S., Taylor, S. E. M., Fingleton, B., Kassiri, Z., Sanchez, O. H., . . . Yeh, W.-C. (2004). Abnormal TNF activity in Timp3−/− mice leads to chronic hepatic inflammation and failure of liver regeneration. *Nature genetics, 36*(9), 969-977.

Mu, D., Cambier, S., Fjellbirkeland, L., Baron, J. L., Munger, J. S., Kawakatsu, H., . . . Nishimura, S. L. (2002). The integrin alpha(v)beta8 mediates epithelial homeostasis through MT1-MMP-dependent activation of TGF-beta1. *The Journal of cell biology, 157*(3), 493-507. doi:10.1083/jcb.200109100 [doi]

Murphy, G. (2011). Tissue inhibitors of metalloproteinases. *Genome biology, 12*(11), 1.

Murphy, G., Houbrechts, A., Cockett, M. I., Williamson, R. A., O'Shea, M., & Docherty, A. J. P. (1991). The N-terminal domain of tissue inhibitor of metalloproteinases retains metalloproteinase inhibitory activity. *Biochemistry, 30*(33), 8097-8102.

Murthy, A., Shao, Y. W., Defamie, V., Wedeles, C., Smookler, D., & Khokha, R. (2012). Stromal TIMP3 regulates liver lymphocyte populations and provides protection against Th1 T cell-driven autoimmune hepatitis. *Journal of immunology (Baltimore, Md.: 1950), 188*(6), 2876-2883. doi:10.4049/jimmunol.1102199 [doi]

Nagase, H., Visse, R., & Murphy, G. (2006). Structure and function of matrix metalloproteinases and TIMPs. *Cardiovascular research, 69*(3), 562-573. doi:S0008-6363(05)00565-1 [pii]

[neural control and coordination - Online CBSE textbooks]). Web Page.

[New Page 1]). Web Page.

Niyibizi, C., Wang, S., Mi, Z., & Robbins, P. D. (2004). Gene therapy approaches for osteogenesis imperfecta. *Gene therapy, 11*(4), 408-416.

Nyman, J. S., Roy, A., Shen, X., Acuna, R. L., Tyler, J. H., & Wang, X. (2006). The influence of water removal on the strength and toughness of cortical bone. *Journal of Biomechanics, 39*(5), 931-938.

Oatley, C. W., Nixon, W. C., & Pease, R. F. W. (1966). Scanning electron microscopy. *Advances in Electronics and Electron Physics, 21*, 181-247.

Ohuchi, E., Imai, K., Fujii, Y., Sato, H., Seiki, M., & Okada, Y. (1997). Membrane type 1 matrix metalloproteinase digests interstitial collagens and other extracellular matrix macromolecules. *The Journal of biological chemistry, 272*(4), 2446-2451.

Opdenakker, G., Van den Steen, P. E., & Van Damme, J. (2001). Gelatinase B: a tuner and amplifier of immune functions. *Trends in immunology, 22*(10), 571-579.

Ou-Yang, H., Paschalis, E. P., Mayo, W. E., Boskey, A. L., & Mendelsohn, R. (2001). Infrared microscopic imaging of bone: spatial distribution of CO32−. *Journal of Bone and Mineral Research, 16*(5), 893-900.

Pettitt, S. J., Liang, Q., Rairdan, X. Y., Moran, J. L., Prosser, H. M., Beier, D. R., . . . Skarnes, W. C. (2009). Agouti C57BL/6N embryonic stem cells for mouse genetic resources. *Nature methods, 6*(7), 493-495. doi:10.1038/nmeth.1342 [doi]

Pillion, J. P., & Shapiro, J. (2008). Audiological findings in osteogenesis imperfecta. *Journal of the American Academy of Audiology, 19*(8), 595-601.

Pillion, J. P., Vernick, D., & Shapiro, J. (2011). Hearing loss in osteogenesis imperfecta: characteristics and treatment considerations. *Genetics research international, 2011*.

[Pix For > Cancellous Bone Tissue]). Web Page.

Power, J., Loveridge, N., Lyon, A., Rushton, N., Parker, M., & Reeve, J. (2003). Bone remodeling at the endocortical surface of the human femoral neck: a mechanism for regional cortical thinning in cases of hip fracture. *Journal of Bone and Mineral Research, 18*(10), 1775-1780.

Qi, J. H., Ebrahem, Q., Moore, N., Murphy, G., Claesson-Welsh, L., Bond, M., . . . Anand-Apte, B. (2003). A novel function for tissue inhibitor of metalloproteinases-3 (TIMP3): inhibition of angiogenesis by blockage of VEGF binding to VEGF receptor-2. *Nature medicine, 9*(4), 407-415.

Rauch, F., & Glorieux, F. H. (2004). Osteogenesis imperfecta. *The Lancet, 363*(9418), 1377-1385.

Rich, A., & Crick, F. H. (1955). The structure of collagen. *Nature, 176*(4489), 915-916.

Ridler, T. W., & Calvard, S. (1978). Picture thresholding using an iterative selection method. *IEEE trans syst Man Cybern, 8*(8), 630-632.

Riedner, E. D., Levin, L. S., & Holliday, M. J. (1980). Hearing patterns in dominant osteogenesis imperfecta. *Archives of Otolaryngology, 106*(12), 737-740.

Ritchie, R. O., Koester, K. J., Ionova, S., Yao, W., Lane, N. E., & Ager, J. W. (2008). Measurement of the toughness of bone: a tutorial with special reference to small animal studies. *Bone, 43*(5), 798-812.

Sabokbar, A., Millett, P. J., Myer, B., & Rushton, N. (1994). A rapid, quantitative assay for measuring alkaline phosphatase activity in osteoblastic cells in vitro. *Bone and mineral, 27*(1), 57-67.

Safadi, F. F., Barbe, M. F., Abdelmagid, S. M., Rico, M. C., Aswad, R. A., Litvin, J., & Popoff, S. N. (2009). Bone structure, development and bone biology. In *Bone pathology* (pp. 1-50): Springer.

Sahebjam, S., Khokha, R., & Mort, J. S. (2007). Increased collagen and aggrecan degradation with age in the joints of Timp3−/− mice. *Arthritis & Rheumatism, 56*(3), 905-909.

Schmid, B., Schindelin, J., Cardona, A., Longair, M., & Heisenberg, M. (2010). A high-level 3D visualization API for Java and ImageJ. *BMC bioinformatics, 11*(1), 1.

Schneider, P., Stauber, M., Voide, R., Stampanoni, M., Donahue, L. R., & Müller, R. (2007). Ultrastructural properties in cortical bone vary greatly in two inbred strains of mice as assessed by synchrotron light based micro-and nano-CT. *Journal of Bone and Mineral Research, 22*(10), 1557-1570.

Seccareccia, E., Pinard, M., Wang, N., Li, S., Burnier, J., Dankort, D., & Brodt, P. (2014). The inhibitor of kappa B kinase-epsilon regulates MMP-3 expression levels and can promote lung metastasis. *Oncogenesis, 3*(8), e116.

Shapiro, J. R., Pikus, A., Weiss, G., & Rowe, D. W. (1982). Hearing and middle ear function in osteogenesis imperfecta. *Jama, 247*(15), 2120-2126.

Shigdel, R., Osima, M., Ahmed, L. A., Joakimsen, R. M., Eriksen, E. F., Zebaze, R., & Bjørnerem, Å. (2015). Bone turnover markers are associated with higher cortical porosity, thinner cortices, and larger size of the proximal femur and non-vertebral fractures. *Bone, 81*, 1-6.

Smith, D. R., Morgan, R. L., & Loewenstein, E. V. (1968). Comparison of the Radiance of Far-Infrared Sources. *JOSA, 58*(3), 433-434.

Spevak, L., Flach, C. R., Hunter, T., Mendelsohn, R., & Boskey, A. (2013). Fourier transform infrared spectroscopic imaging parameters describing acid phosphate substitution in biologic hydroxyapatite. *Calcified tissue international, 92*(5), 418-428.

Stamenkovic, I. (2003). Extracellular matrix remodelling: the role of matrix metalloproteinases. *The Journal of pathology, 200*(4), 448-464.

Stewart, E. J., & O'Reilly, B. F. (1989). A clinical and audiological investigation of osteogenesis imperfecta. *Clinical Otolaryngology & Allied Sciences, 14*(6), 509-514.

Suzuki, M., Raab, G., Moses, M. A., Fernandez, C. A., & Klagsbrun, M. (1997). Matrix metalloproteinase-3 releases active heparin-binding EGF-like growth factor by cleavage at a specific juxtamembrane site. *Journal of Biological Chemistry, 272*(50), 31730-31737.

Swinnen, F. K. R., De Leenheer, E. M. R., Coucke, P. J., Cremers, C. W. R. J., & Dhooge, I. J. M. (2009). Audiometric, surgical, and genetic findings in 15 ears of patients with osteogenesis imperfecta. *The Laryngoscope, 119*(6), 1171-1179.

Turner, C. H., & Burr, D. B. (1993). Basic biomechanical measurements of bone: a tutorial. *Bone, 14*(4), 595-608.

Unnanuntana, A., Rebolledo, B. J., Khair, M. M., DiCarlo, E. F., & Lane, J. M. (2011). Diseases affecting bone quality: beyond osteoporosis. *Clinical Orthopaedics and Related Research®, 469*(8), 2194-2206.

Ural, A., & Vashishth, D. (2007). Effects of Intracortical Porosity on Fracture Toughness in Aging Human Bone: A μCT-Based Cohesive Finite Element Study. *Journal of Biomechanical Engineering, 129*(5), 625-631.

Van Bezooijen, R. L., Papapoulos, S. E., Hamdy, N. A., Ten Dijke, P., & Löwik, C. W. (2005). Control of bone formation by osteocytes? lessons from the rare skeletal disorders sclerosteosis and van Buchem disease. *BoneKEy-Osteovision, 2*(12), 33-38.

Vardakastani, V., Saletti, D., Skalli, W., Marry, P., Allain, J. M., & Adam, C. (2014). Increased intra-cortical porosity reduces bone stiffness and strength in pediatric patients with osteogenesis imperfecta. *Bone, 69*, 61-67. doi:10.1016/j.bone.2014.09.003

Varghese, S. (2006). Matrix metalloproteinases and their inhibitors in bone: an overview of regulation and functions. *Frontiers in bioscience : a journal and virtual library, 11*, 2949-2966. doi:2024 [pii]

Vatsa, A., Breuls, R. G., Semeins, C. M., Salmon, P. L., Smit, T. H., & Klein-Nulend, J. (2008). Osteocyte morphology in fibula and calvaria—is there a role for mechanosensing? *Bone, 43*(3), 452-458.

Verrier, S., Hogan, A., McKie, N., & Horton, M. (2004). ADAM gene expression and regulation during human osteoclast formation. *Bone, 35*(1), 34-46.

Verstappen, J., & Von den Hoff, J. W. (2006). Tissue inhibitors of metalloproteinases (TIMPs): their biological functions and involvement in oral disease. *Journal of dental research, 85*(12), 1074-1084. doi:85/12/1074 [pii]

Viguet-Carrin, S., Garnero, P., & Delmas, P. D. (2006). The role of collagen in bone strength. *Osteoporosis International, 17*(3), 319-336.

Visse, R., & Nagase, H. (2003). Matrix metalloproteinases and tissue inhibitors of metalloproteinases: structure, function, and biochemistry. *Circulation research, 92*(8), 827-839. doi:10.1161/01.RES.0000070112.80711.3D [doi]

Watterson, T. (2013). The Extracellular Matrix, Matrix Metalloproteinases and their roles in Disease.

Weiner, S., & Traub, W. (1986). Organization of hydroxyapatite crystals within collagen fibrils. *FEBS letters, 206*(2), 262-266.

Weiner, S., Traub, W., & Wagner, H. D. (1999). Lamellar bone: structure–function relations. *Journal of structural biology, 126*(3), 241-255.

Weiner, S., & Wagner, H. D. (1998). The material bone: structure-mechanical function relations. *Annual Review of Materials Science, 28*(1), 271-298.

Whitelock, J. M., Murdoch, A. D., Iozzo, R. V., & Underwood, P. A. (1996). The degradation of human endothelial cell-derived perlecan and release of bound basic fibroblast growth factor by stromelysin, collagenase, plasmin, and heparanases. *The Journal of biological chemistry, 271*(17), 10079-10086.

Wojtowicz-Praga, S. M., Dickson, R. B., & Hawkins, M. J. (1997). Matrix metalloproteinase inhibitors. *Investigational new drugs, 15*(1), 61-75.

Xu, J., Rodriguez, D., Petitclerc, E., Kim, J. J., Hangai, M., Moon, Y. S., . . . Brooks, P. C. (2001). Proteolytic exposure of a cryptic site within collagen type IV is required for angiogenesis and tumor growth in vivo. *The Journal of cell biology, 154*(5), 1069-1079. doi:10.1083/jcb.200103111 [doi]

Xu, L., Huang, X., Ta, N., Rao, Z., & Tian, J. (2015). FINITE ELEMENT MODELING OF THE HUMAN COCHLEA USING FLUID–STRUCTURE INTERACTION METHOD. *Journal of Mechanics in Medicine and Biology, 15*(03), 1550039.

Yeni, Y. N., Brown, C. U., Wang, Z., & Norman, T. L. (1997). The influence of bone morphology on fracture toughness of the human femur and tibia. *Bone, 21*(5), 453-459.

Yu, Q., & Stamenkovic, I. (2000). Cell surface-localized matrix metalloproteinase-9 proteolytically activates TGF-beta and promotes tumor invasion and angiogenesis. *Genes & development, 14*(2), 163-176.

Zhang, H., Doty, S. B., Hughes, C., Dempster, D., & Camacho, N. P. (2007). Increased resorptive activity and accompanying morphological alterations in osteoclasts derived from the oim/oim mouse model of osteogenesis imperfecta. *J Cell Biochem, 102*(4), 1011-1020. doi:10.1002/jcb.21337

Appendix A: Matlab Script

A.1 Matlab Script to Analyze Mechanical and Material Properties

```
clc,clear,close all
folderName = uigetdir('','Select MECHANICAL DATA FOLDER');
folderName1 = uigetdir('','Select GEOMETRIC DATA FOLDER');
folderName2 = uigetdir('','Select folder for SAVING RESULTS');
directoryName = fullfile(folderName,'*.xlsx');
excelFiles = dir(directoryName);
numberFiles = length(excelFiles);
directoryName1 = fullfile(folderName1,'*.xlsx');
excelFiles1 = dir(directoryName1);
%% Humeri Analysis
l = 9;
fileName1 = fullfile(folderName1, excelFiles1(1).name);
excelData1 = xlsread(fileName1);
CSA = excelData1(:,1);
diameter = excelData1(:,2);
MOI = excelData1(:,3);
for i = 1:numberFiles

    fileName = fullfile(folderName, excelFiles(i).name);
    excelData = xlsread(fileName);
    extension = excelData(:,1);
    load = excelData(:,2);

    for j = 1:length(load)
        if load(j) >= 0.5
            startPoint = j;
            break
        end
    end
    extension = extension(startPoint:end)-extension(startPoint);
    load = load(startPoint:end)-load(startPoint);
    figure(i);
    plot(extension,load);
    title(excelFiles(i).name(1:3));
    xlabel('Extension (mm)');
    ylabel('Load (N)');
    [extensionPoints, loadPoints] = ginput(2);
    for j = 1:length(extension)
       if extension(j) >= extensionPoints(1)
           linearStart = j;
           break
       end
    end
    for j = 1:length(extension)
       if extension(j) >= extensionPoints(2)
           linearEnd = j;
           break
       end
    end
```

```
    linearFit =
polyfit(extension(linearStart:linearEnd),load(linearStart:linearEnd
),1);
    m = linearFit(1);
    b = linearFit(2);
    linearCurve = m*(extension-(0.002))+(b);
    figure(i);
    hold on
    plot(extension,load);
    plot(extension,linearCurve,'r');
    title(excelFiles(i).name(1:3));
    xlabel('Extension (mm)');
    ylabel('Load (N)');
    hold off
    for j = length(load):-1:1
        if linearCurve(j) <= load(j)
            yieldPoint = j;
            break
        end
    end
    stiffness = m;
    yieldLoad = load(yieldPoint);
    ultimateLoad = max(load);
    energyYield =
trapz(extension(1:yieldPoint),load(1:yieldPoint));
    energyFailure = trapz(extension,load);
    yieldStress = (yieldLoad*l*(diameter(i)/2))/(4*MOI(i));
    ultimateStress = (ultimateLoad*l*(diameter(i)/2))/(4*MOI(i));
    youngsModulus = m*(l^3)/(48*(MOI(i)));
    results(i,1) = stiffness;
    results(i,2) = yieldLoad;
    results(i,3) = ultimateLoad;
    results(i,4) = energyYield;
    results(i,5) = energyFailure;
    results(i,6) = youngsModulus/1000;
    results(i,7) = yieldStress;
    results(i,8) = ultimateStress;
end
fileName2 = strcat('Results','.xlsx');
xlswrite(fullfile(folderName2,fileName2),results,1,'A1');

%% Vertebrae Analysis
fileName1 = fullfile(folderName1, excelFiles1(1).name);
excelData1 = xlsread(fileName1);
CSA = excelData1(:,1);
l = excelData1(:,2);
for i = 1:numberFiles

    fileName = fullfile(folderName, excelFiles(i).name);
    excelData = xlsread(fileName);
    extension = excelData(:,1);
    load = excelData(:,2);

    for j = 1:length(load)
```

```
        if load(j) >= 0.5
            startPoint = j;
            break
        end
    end
    extension = extension(startPoint:end)-extension(startPoint);
    load = load(startPoint:end)-load(startPoint);
    figure(i);
    plot(extension,load);
    title(excelFiles(i).name(1:3));
    xlabel('Extension (mm)');
    ylabel('Load (N)');
    [extensionPoints, loadPoints] = ginput(2);
    for j = 1:length(extension)
       if extension(j) >= extensionPoints(1)
           linearStart = j;
           break
       end
    end
    for j = 1:length(extension)
       if extension(j) >= extensionPoints(2)
           linearEnd = j;
           break
       end
    end
    linearFit =
polyfit(extension(linearStart:linearEnd),load(linearStart:linearEnd
),1);
    m = linearFit(1);
    b = linearFit(2);
    linearCurve = m*(extension-(0.002))+(b);
    figure(i);
    hold on
    plot(extension,load);
    plot(extension,linearCurve,'r');
    title(excelFiles(i).name(1:3));
    xlabel('Extension (mm)');
    ylabel('Load (N)');
    hold off
    for j = length(load):-1:1
        if linearCurve(j) <= load(j)
            yieldPoint = j;
            break
        end
    end
    stiffness = m;
    yieldLoad = load(yieldPoint);
    ultimateLoad = max(load);
    energyYield =
trapz(extension(1:yieldPoint),load(1:yieldPoint));
    energyFailure = trapz(extension,load);
    yieldStress = (yieldLoad/(CSA(i)));
    ultimateStress = (ultimateLoad/(CSA(i)));
    youngsModulus = (m*(l(i)/(CSA(i))));
```

```
    results(i,1) = stiffness;
    results(i,2) = yieldLoad;
    results(i,3) = ultimateLoad;
    results(i,4) = energyYield;
    results(i,5) = energyFailure;
    results(i,6) = youngsModulus/1000;
    results(i,7) = yieldStress;
    results(i,8) = ultimateStress;
end
fileName2 = strcat('Results','.xlsx');
xlswrite(fullfile(folderName2,fileName2),results,1,'A1');
```

Appendix B: ImageJ Subroutines

B.1 Skeletonize3D and Analyze Skeleton

1. Load stack of binary canal images for an entire bone into ImageJ
   File > Import > Image Sequence > {Select first image in file stack} > Set sequence options} > click OK
2. Set background of binary canal images to black (If necessary)
   Edit > Invert > Click Yes
3. Apply morphological filter
   Plugins > MorphoLibJ > Morphological filters 3D > {Set Operation to "Closing"} > {Set Element to Octagon} > {Set radius to 8} > click OK
   Note: These settings were determined by analyzing the original stack of images to determine the volume of the structure and then comparing that value to the values of the resulting volumes obtained from the stacks of images obtained after applying the various object closing algorithms that are available in ImageJ. The particular closing algorithm describe above was chosen because its volume was the closest to the original volume while still removing all the voids in the canals.
4. Skeletonize canals
   Plugins > BoneJ > Skeletonize3D
5. Analyze canals
   Plugins > BoneJ > Analyze Skeleton > {Check "Show Detailed Info"}

B.2 Scale Image Stack

1. Load stack of binary canal images of entire bone into ImageJ
   File > Import > Image Sequence > {Select first image in file stack} > Set sequence options} > click OK
2. Scale Images
   Image > Scale > {Set Scaling Factors for X, Y, and Z axis} > Click OK

   Note: To determine the extent to which a stack of images can be scaled prior to analysis, analyze a portion of the original stack of images and determine the volume of the structure of interest using the particle analyzer subroutine (Plugins > Analyze > Particle Analyzer > {Uncheck all boxes except "Enclosed volume"} Click OK). Then, incrementally scale the image down by factors of 0.1 (X,Y,Z = 0.9, then X,Y,Z = 0.8, etc.) and compare the volumes of the scaled images to the volume of the original stack using the formula:

$$\%\, diff = \left(\frac{Original\ Volume - Scaled\ Volume}{Original\ Volume}\right) * 100$$

   The images can be scaled in size up to a 5% difference in volume between the original volume and the scaled volume. For this thesis, the images were scaled to 0.5 of the original dimensions.